Air Flow Effects in the Piston Ring Pack and their Implications on Oil Transport

by

Yuan Wang

Dipl.-Ing., Universität Stuttgart (2012)

Submitted to the Department of Aeronautics and Astronautics
in partial fulfillment of the requirements for the degree of

Master of Science in Aeronautics and Astronautics

at the

MASSACHUSETTS INSTITUTE OF TECHNOLOGY

September 2012

Author ....
Department of Aeronautics and Astronautics
August 15, 2012

Certified by ....
Tian Tian
Principal Research Engineer, Department of Mechanical Engineering
Thesis Supervisor

Accepted by ....
Eytan H. Modiano
Professor of Aeronautics and Astronautics
Chair, Graduate Program Committee

Air Flow Effects in the Piston Ring Pack and their Implications on Oil Transport

by

Yuan Wang

Submitted to the Department of Aeronautics and Astronautics
on August 15, 2012, in partial fulfillment of the
requirements for the degree of
Master of Science in Aeronautics and Astronautics

Abstract

3 different flow regimes of piston blowby air and their influences on oil transport are studied. It is found that air mainly interacts with oil close to the ring gaps and directly below the ring-liner contacts. Geometric features at the gaps to smoothen airflow and prevent flow detachments can increase blowby mass flow rate and thus drainage oil mass flow rate by up to 60%. Only oil within 1 to 2 gap widths distance from the gaps are transported through the gap by air drag and the engine pressure drop. Downstream of the ring gap, transported oil will either be caught in vortices directly below the ring gaps or pumped into the downstream ring groove due to the creation of a blowby stagnation point. Far away from the gaps, oil is mainly transported in axial direction through the grooves and the piston-liner interface. Low capillary numbers in the order of 10^{-5} indicate close to no oil transport into circumferential direction from blowby shear. The oil transport radially into the grooves is mainly determined by hydrostatics and capillary effects in the groove flanks wheras air in the second land only has an influence on oil transport by preventing bridging after TDC by creating a stagnation point directly below the rings on the liner.

Thesis Supervisor: Tian Tian
Title: Principal Research Engineer, Department of Mechanical Engineering

Acknowledgments

My main acknoledgements go to my brilliant advisor Dr. Tian Tian for his endless support and excellent guidance throughout my research. All my motivation and passion stem from his constant clarity, enthusiasm and experience without which I would have never been able to succeed at MIT.

Furthermore I would like to express all my gratitudes to our sponsors Argonne National Lab, Daimler, DOE, Mahle, Renault, PSA, Toyota, Volkswagen and Volvo, who made this project possible. Specifically I would like to thank Remi for his great humor and training he provided; Bengt, Erich, Hand-Jürgen, Matthias, Paulo and Dr. Fiedler for all the fun discussions and motivation; Steve and Eric for taking care of all necessities and providing feedback and Tom for his constructive suggestions.

Thanks a lot to the funnniest and smartest labmates at MIT Camille, Haijie, Kai, Matthieu and Yang. I love the team natured spirit in our office, the sporadic sweet secrets hidden in our fridge and all the great discussions we had. Nowhere else will it be so fun coming to work every morning. Moreover I would like to thank Janet and Thane for their kindness and assistance during my studies.

Finally I would like to thank my wonderful parents and girlfriend for all their support and love. They have continuously brought joy and laughter to me during my absence and I look forward to spending more time with them in the future.

Contents

List of Figures

List of Tables

Chapter 1

Introduction

1.1 Background

Engine blowby is one of the critical factors for thermodynamic efficiency, oil consumption and engine life cycle. With environmental regulations becoming more restrictive and increases of engine performances becoming more expensive, understanding and regulating engine blowby has become an important factor in designing cleaner and more efficient engines. Because of small size, high unsteadiness and material restrictions it is very difficult to visualize blowby air in an engine. The open source tool OpenFOAM will be used on relevant engine geometry in this thesis to understand the interactions of blowby on oil.

1.1.1 Ring Pack Geometry

The piston head contains 3 rings as seen in figure 1-1. The rings have 3 primary functions

1. Sealing combustion gases
2. Controlling oil consumption
3. Heat transfer between piston and cylinder

Figure 1-1: Piston Head Assembly

The upper two rings are referred to as compression rings and mainly serve to seal the combustion chamber and thus control blowby, which is the gas flow from the combustion chamber into the engine crankcase. The third ring is commonly referred to as oil control ring and mainly serves to distribute a desirable oil film on the cylinder wall, which is referred to as liner, and to limit the oil flow from the crankcase to the combustion chamber. The amount of blowby is mainly determined by the first compression ring.

Figure 1-2 shows a sketch for a cut through the piston with the circumferential vector being the cutting plane's normal vector. The rings are sitting in their respective groove slots on the piston. Since groove dimensions are slightly larger than ring dimensions, the rings do not have a fixed position inside the groove and can either sit on the upper groove flanks or the lower groove flanks, which is determined by pressure, inertia and friction forces on the ring. Moreover axial fluttering and radial collapse situations can occur where additional flow passages for blowby is created, as shown

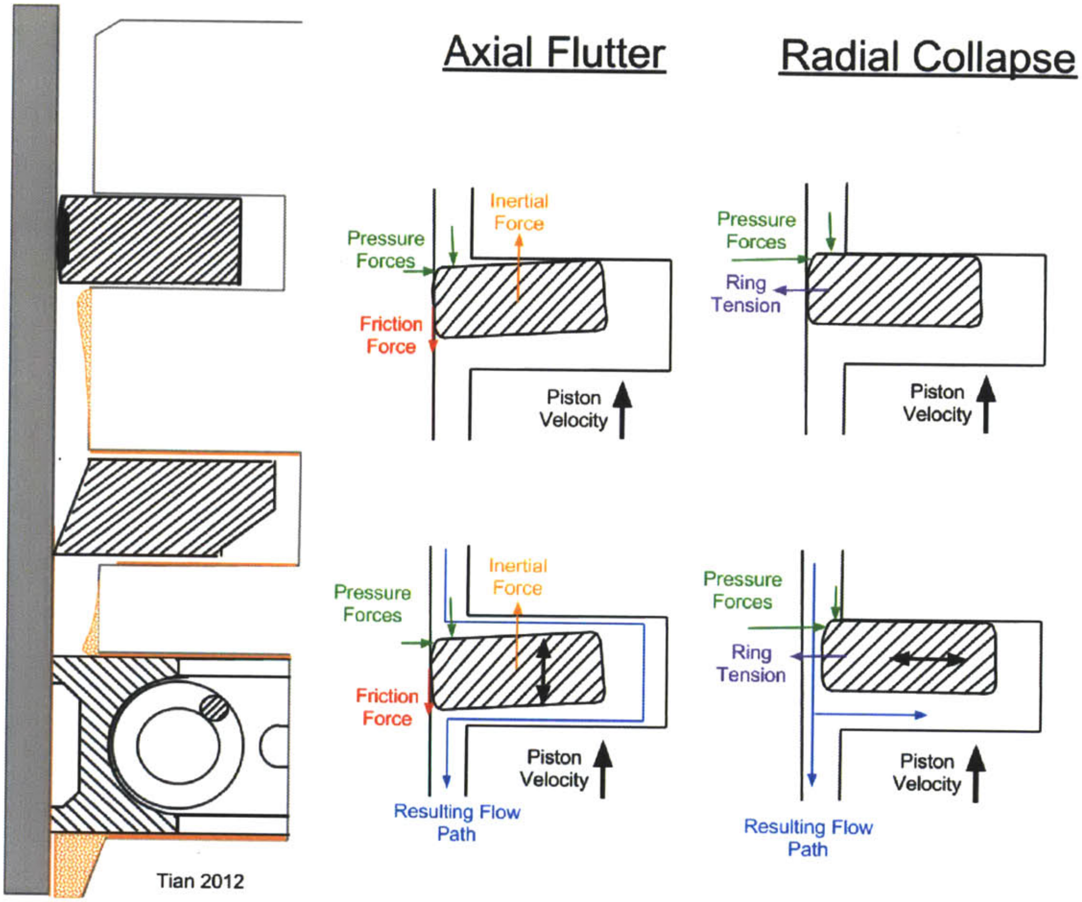

Figure 1-2: Rings sitting in the piston groove and possible instabilities

on the right side of figure 1-2. This work will rather focus on higher load conditions where both cylinder pressure and ring tension are high so that both instabilities are avoided.

1.1.2 Blowby Flow Path in the Piston Ring Pack

There are 3 main flow regimes for blowby as it passes the ring pack:

- the ring gaps, which are characterized by minimum flow areas, thus choking the flow,
- the lands between piston and liner in which the blowby has small velocities in circumferential direction and

- the lands in which the blowby is dragged by liner as the piston moves up and down, similar to cavity flows.

A sample sketch of the blowby flow path inside the ring pack is shown in figure 1-3, where gap flows are in orange, circumferential flows are in blue and cavity type flows in red. Ring Gap flows are mainly characterized by minimum flow areas inside the ring pack which choke the flow during most crank angles.

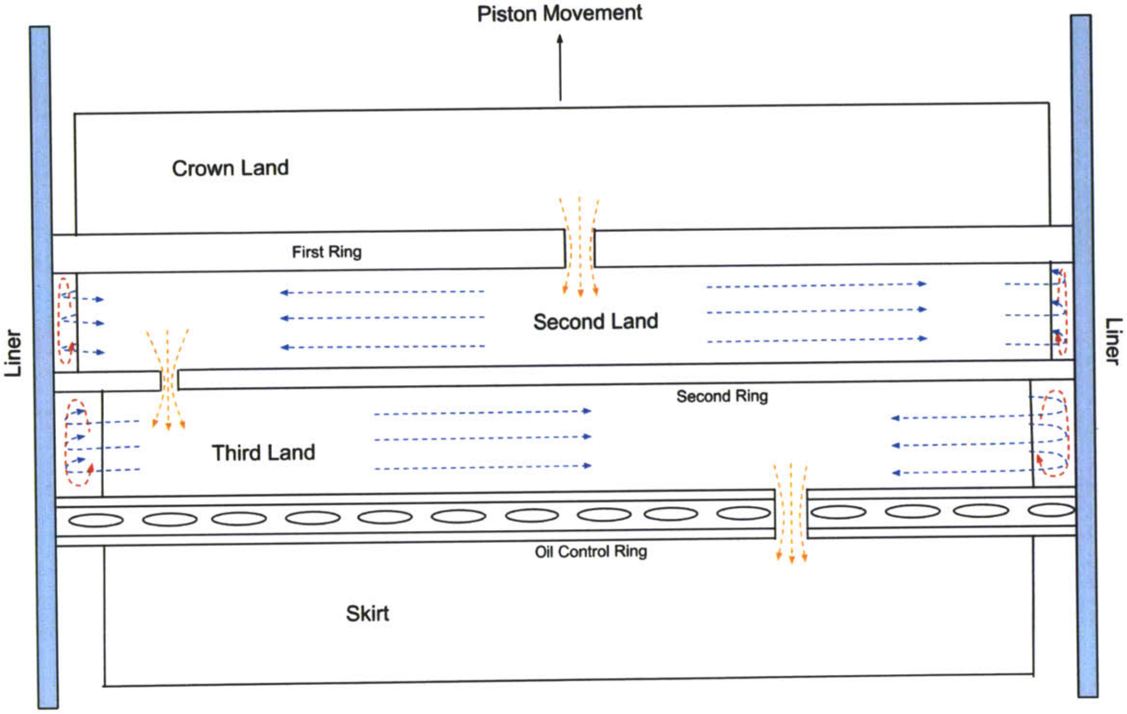

Figure 1-3: Flow regimes in the ring pack

Circumferential flows in the lands are fairly slow flows due to the total pressure loss after the ring gaps and the large area expansion. In the second land, the cross sectional flow area normal to circumferential flow direction is 2 orders of magnitues larger than the gap area, which will cause velocities to drop by 2 orders of magnitude.

Cross sectional flows in the lands are cavity types of flows which get dragged by the liner as the piston moves up and down in the cylinder.

This work investigates each of the 3 types of flows from upstream to downstream, starting at the first ring gap, continuing into the circumferential flow in the second land and concluding in the third land cross section.

1.2 Motivation and Objectives

This work aims at

1. estimating relevant flow parameters
2. developing qualitative and quantitative insight into different flow regimes and
3. couple theoretical findings with high fidelity CFD calculations

This will allow engine designers to understand critical oil transport mechanism to control and reduce oil consumption. At the start of each chapter, a more detailed overview on specific objectives for the respectively discussed flow regime will be given.

1.3 Related Research

Tian et al. [11] estimated gas flow through ring gaps using an isentropic orifice flow relationship

$$\dot{m}_{gap} = \frac{C_D A_{gap} p_U}{\sqrt{RT_U}} f_m \tag{1.1}$$

with

$$f_m = \sqrt{\gamma}\left(\frac{2}{\gamma+1}\right)^{(\gamma+1)/2(\gamma-1)} \tag{1.2}$$

for choked flow and

$$C_D = 0.85 - 0.25PR^2 \tag{1.3}$$

from experimental data (Shapiro [9]), where PR is the downstream to upstream static pressure ratio.

Senzer [8] showed the relationship of drained oil mass flow rate and blowby volume flow rate in the oil control ring (OCR) groove by assuming a parallel separated two-phase flow without mixing. Combining a Poiseuille type of flow for high inertia blowby air and a Couette type of flow for the dragged oil, the mass flow rate relationship of both phases becomes

$$\dot{m}_{oil} \approx \rho_{air} Q_{Blowby} \frac{\nu_{air}}{\nu_{oil}} \left(\frac{\beta}{1-\beta}\right)^2 \tag{1.4}$$

where β represents the non-dimensionalized oil height in the OCR groove $\beta = \frac{h_{oil}}{H_{OCR}}$. This proportional relationship is in good accordance to measurements carried out in the MIT - Sloan Automotive Lab.

Chapter 2

Air flow through ring gaps

In chapter 1.1.2 it was stated that the first ring gap is the main mechanism of controlling blowby because of the flow choking. The main focus in this chapter lies in the investigation of geometric and thermophysical parameters on the amount of blowby mass flow with the overall aim for designers to understand and control blowby. Moreover implications on oil transport are gained by looking at flow patterns at the gap.

2.1 Definition of Test Cases

2.1.1 Choking at the first Ring Gap

For the choked flow assumption to be true, the corrected flow per unit area

$$D = \frac{\dot{m}_{gap}\sqrt{RT_t}}{A^* p_t \sqrt{\gamma}}, \tag{2.1}$$

which is described in detail by Greitzer et al. [1], must have a global maximum at the first ring gap, as shown in figure 2-1, where the corrected flow per unit area against Mach number is plotted. The whole ring pack can be simplified to a series of 3 nozzles, each representing one ring gap, with subsequent sudden expansions as sketched on figure 2-2. For the first nozzle to choke, the condition

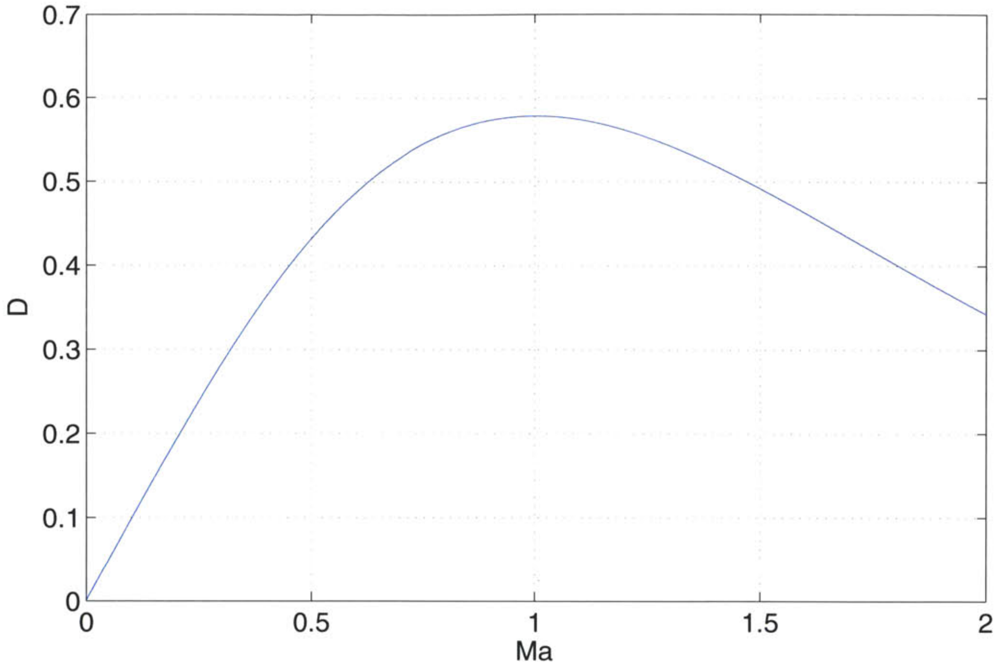

Figure 2-1: Corrected Flow per Unit Area

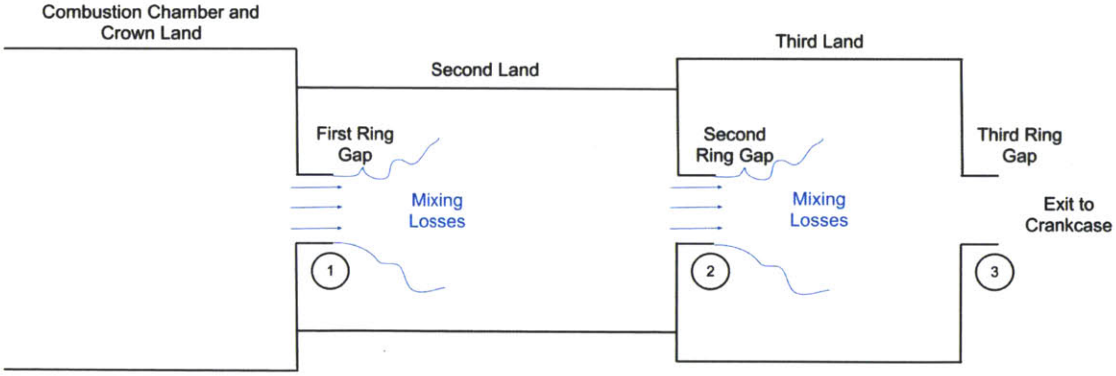

Figure 2-2: Ring Pack Simplification

$$D_1 > D_2, D_1 > D_3 \tag{2.2}$$

must hold, or similarly by assuming constant gas values and no heat transfer

$$\frac{D_1}{D_2} \leq \frac{p_{t2}A_2}{p_{t1}A_1}, \frac{D_1}{D_3} \leq \frac{p_{t3}A_3}{p_{t1}A_1} \tag{2.3}$$

because $\dot{m}$ has to be constant in all 3 nozzles in the steady-state case due to continuity. For very large area ratios at the sudden expansions entropy is generated due to mixing and the resulting stagnation pressure loss is almost as large as the whole dynamic pressure, which has been shown for example by Ward-Smith [12]. That means that the stagnation pressure p_{t2} scales as

$$p_{t2} = p_{t1} - \frac{1}{2}\rho U_1^2 = p_1 \tag{2.4}$$

and the stagnation pressure ratio scales as

$$\frac{p_{t2}}{p_{t1}} = \frac{p_1}{p_{t1}} = \left(1 + \frac{\gamma - 1}{2} Ma^2\right)^{-\frac{\gamma}{\gamma - 1}} \tag{2.5}$$

For Mach numbers in the order of 10^{-1} and 10^{0} the stagnation pressure ratio p_{t2}/p_{t1} typically varies from 0.5 to 1 and p_{t3}/p_{t1} varies from 0.25 to 1, whereas both area ratios A_2/A_1 and A_3/A_1 are usually always in the order of 5 or larger due to the large clearances d in subsequent lands. This simple scaling shows that

$$\frac{D_1}{D_2} \leq 1, \frac{D_1}{D_3} \leq 1 \tag{2.6}$$

and thus choking at the first ring gap always occurs. This has been shown by pressure measurements in the Sloan Automotive Lab as well.

2.1.2 Relevant Geometry

Upper Compression Ring

In the case where friction and inertia push the ring towards the upper flank it is easy to determine the minimum blowby flow area as the gap cross sectional area in axial direction. During combustion, the pressure ratio across the ring is very large and the ring mostly sits on the lower flank of the groove. In this case it becomes unclear where the minimal flow area is and this study will focus on that type of situation. The resulting flow sections inside the groove are outlined in figure 2-3. Typical gap

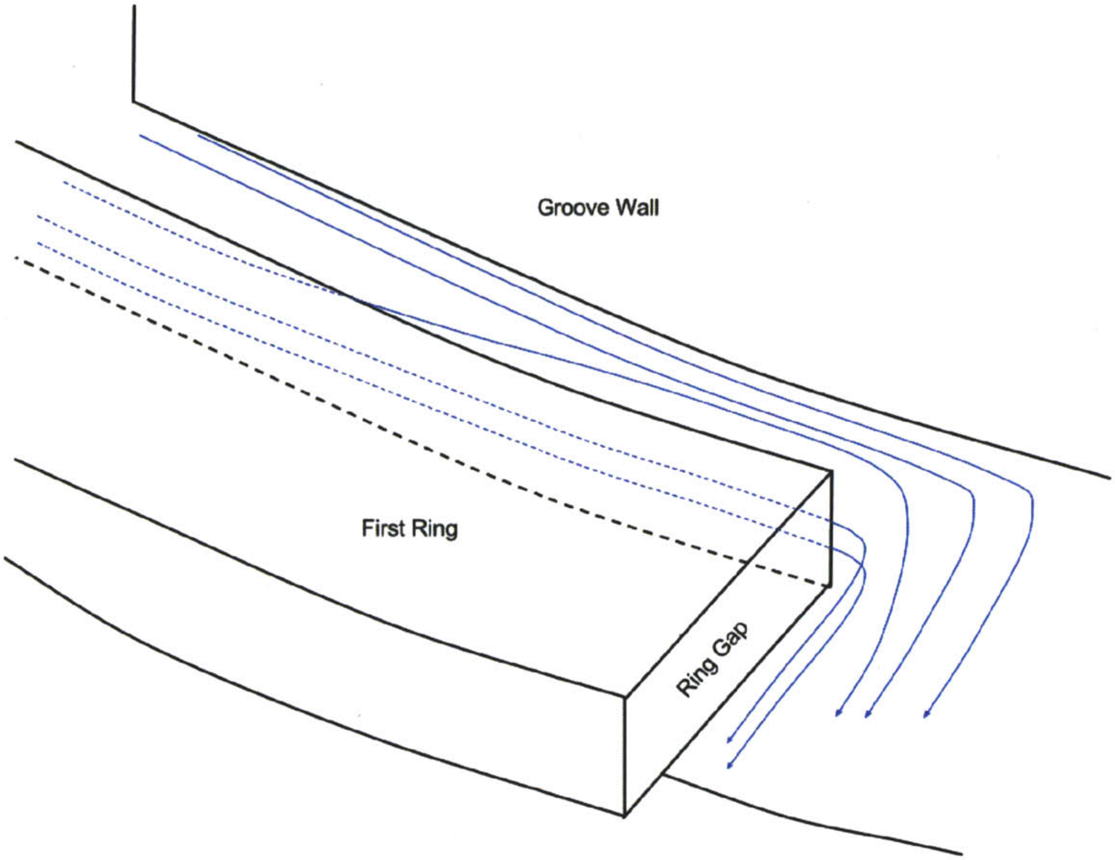

Figure 2-3: Possible Flow Path in the Piston Groove

widths L range from $0.2mm$ to $0.4mm$. Here, a gap width of $0.3mm$ is chosen.

Chamfer and Land Clearance

One of the features of the piston is its chamfer below the first ring, as shown in figure 2-4. Previous experiments and real world cases have indicated that size and shape

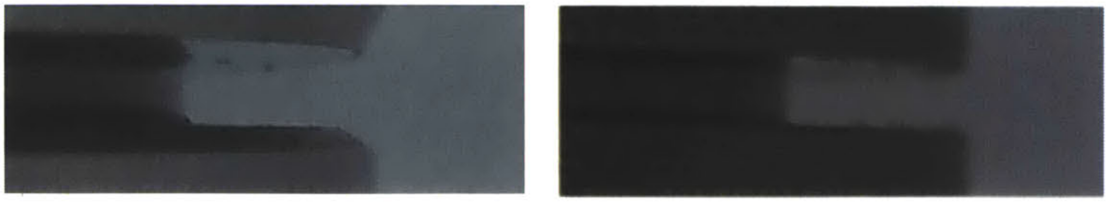

Figure 2-4: Piston groove with (right) and without chamfer

of the chamfer have a significant impact on the magnitude of blowby mass flow rate.

The chamfer angle is typically 45^o whereas its depth c, as shown in figure 2-5, can vary from engine to engine. Variations in chamfer size from $10\mu m$ to $100\mu m$ are carried out in this work to study its effect on blowby. Because the piston can tilt and expand under different thermal conditions than the liner, the clearance between the piston land and the liner can vary during an engine's operating cycle and life. Typical values for the clearance in the second land d range from $100\mu m$ to $200\mu m$, for which this study will be conducted.

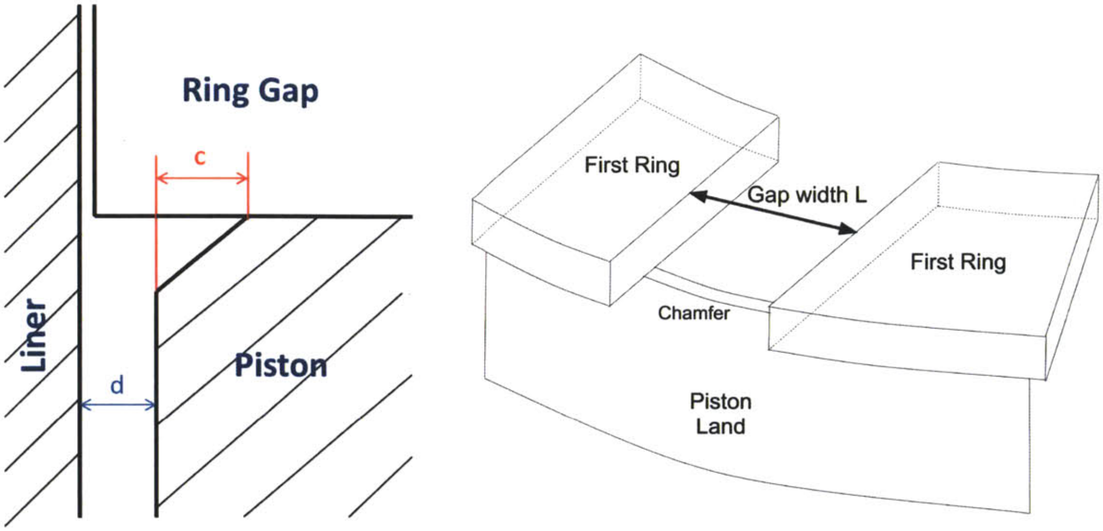

Figure 2-5: Sketch of the Ring Gap

2.1.3 Computational Domain

The first area in the engine where flow parameters are definitely known is in the combustion chamber, where we can consider the flow at rest with a given total temperature T_t and total pressure p_t. This is represented as a classical plenum. Given the overall objective of determining the blowby air flow rate, only the flow at the first ring gap where minimal flow area occurs is of interest because choking limits the mass flow rate, rendering the flow downstream of the choking spot of no interest for this study. The difficulty is the definition of the actual minimum flow area when there is a chamfer below the ring gap. For this reason the domain is extended far away from the ring gap to allow the flow to fully development right after the gap, such that partial derivatives of flow parameters normal to the boundary $\frac{\partial}{\partial \vec{n}}$ disappear to make use of Neumann boundary conditions. The finalized complete computation domain is shown in figure 2-6 that represents a plenum flow out of a converging nozzle into a given atmospheric pressure, which is the static pressure of the piston first land. This plenum flow configuration is further expanded with a groove section as shown on the right side of figure 2-6.

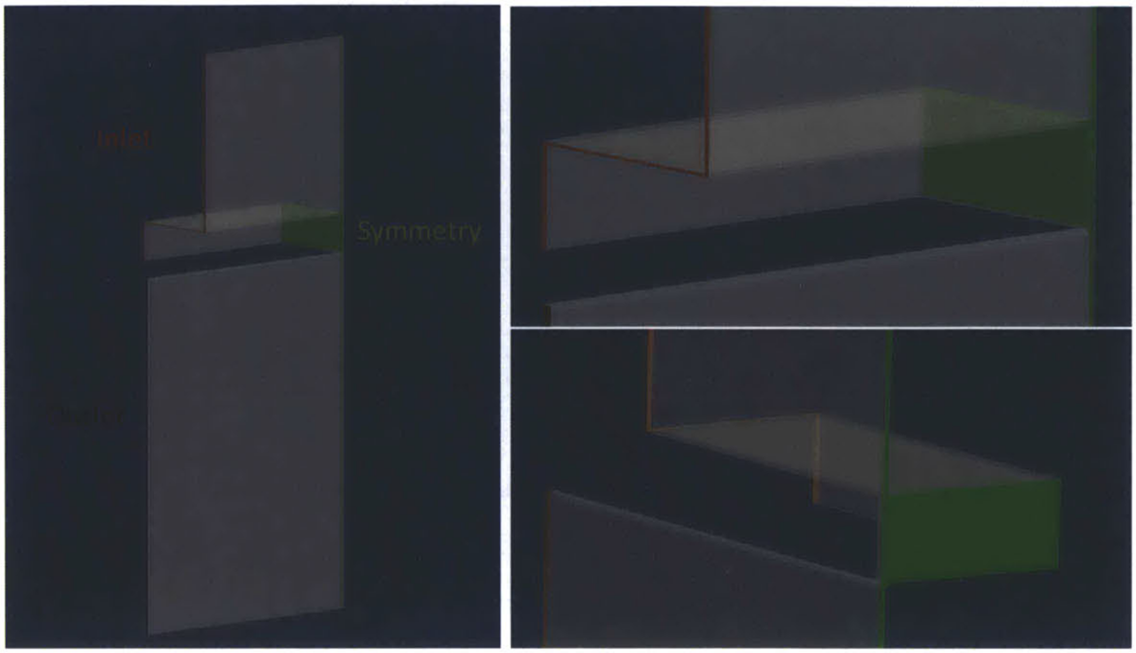

Figure 2-6: Computational Domain

2.1.4 Relevant Parameters

From compressible flow theory it is known that the air mass flow rate is determined by gas properties, upstream stagnation values and geometry. In the given cases the mass flow rate $\dot{m}_{gap}$ of blowby air with air properties R and γ depends on the plenum stagnation values p_t T_t and the minimum flow area A^*, which depends on the two geometric parameters c and d. From dimensional analysis we obtain the two non-dimensional products D and

$$C = \frac{c}{d} \tag{2.7}$$

where C is a geometric parameter and D is the aforementioned corrected flow per unit area. As previously stated, predicting the choking area A^* a priori is very difficulty and thus the area $A_{ref} = L{\cdot}d$ is used for the choking area. A more thorough discussion on the that area will be given in section 2.3 when results are discussed.

Given the calculation ranges as described in section 2.1.2, this study varies C from 0.05 to 1. To summarize, all test cases for geometric variations are listed in table 2.1

	$c = 10\mu m$	$c = 40\mu m$	$c = 70\mu m$	$c = 100\mu m$
$d = 100\mu m$	$C = 0.1$	$C = 0.4$	$C = 0.7$	$C = 1$
$d = 150\mu m$	$C = 0.067$	$C = 0.267$	$C = 0.467$	$C = 0.667$
$d = 200\mu m$	$C = 0.05$	$C = 0.2$	$C = 0.35$	$C = 0.5$

Table 2.1: Geometric Variations for Test Cases

2.1.5 Boundary Conditions

There are 4 different boundary types used in this study:

- The inlet plenum is specified by stationary flow and its stagnation values.
    - Since the main idea is to choke the flow, a sufficiently large total to static pressure ratio is chosen to just choke the flow since large pressure ratios will cause an increase in computational residuals. Although absolute mass flow is dependent on p_t and T_t, the previous non-dimensionalization will cause the corrected flow per unit area to be the same maximum value whenever choking occurs and thus should make variations in p_t and T_t unnecessary.
    - To verify this non-dimensionalization effect, calculations with variations in the combustion temperature T_t are conducted for a range from $400K$ to $2000K$ and later verified to expected values.
    - Setting a fixed value of 0m/s caused difficulties in converging the calculation since it sets a fixed constraint on the flow boundary. At the vicinity of the inlet corner singularity, flow from the top boundary can enter the

left inlet boundary and vice versa. This will cause either non-zero velocities and a subsequent crash in the calculation or an artifical creation of a velocity-pressure wave. Both effects are undesired and thus the boundary condition *pressureInletOutletVelocity* is chosen to allow some backflow at the corner region. For an inflow condition the velocity is obtained using the flux from the first adjacent cell of the boundary.

- As mentioned in section 2.1.3 the outlet is far away so that Neumann boundary conditions for temperature and velocity hold for the fully developed flow. The pressure is specified as Dirichlet condition to meet the critical pressure ratio. Theoretically, the first law states that the total temperature in the flow field must remain constant because this case does not involve heat or work addition. This implies that setting a Dirichlet condition on the total temperature at the outlet to match inlet and outlet T_t sets a perfect constraint on the temperature field. In practical usage, this idea is soon discarded because a Dirichlet type of boundary condition sets a very strict constraint on the calculation and slight mistakes by the solver render a full convergence very difficult. Indeed, setting only one dirichlet condition on both pressure sides already causes the case to be difficult to converge.

- For simplification, the effects of heat transfer on choking are taken out by using adiabatic walls. It can be expected that heat addition would increase the total temperature and thus cause the flow to choke earlier, decreasing the amount of blowby. This effect is already described in detail by Greitzer et al. [1] and could possibly be included in further studies in the future.

- To save computational time, the symmetric ring gap geometry is split in half with the symmetry boundary condition at the plane of symmetry.

All boundary conditions are summed up in table 2.2

2.1.6 Gas Properties and Flow Regime

A single phase perfect gas with air properties is chosen as working fluid. For more realistic calculations, fuel-air mixture properties might be more appropriate, especially under heavy load conditions. The gas values are kept constant with dynamic viscosity $\mu = 2.3 \cdot 10^{-5} kg/m \cdot s$, Prandtl number $Pr = 0.7$, heat capacity $c_p = 1007 J/kg \cdot K$ and specific gas constant $R = 287 J/kg \cdot K$. Using the same non-dimensionalizing argument as for total pressure, these values are kept constant throughout the whole study.

Estimating the Reynolds number inside the combustion chamber

$$Re_{max\_plenum} \approx \frac{UL}{\nu} \approx \frac{10^13 \cdot 10^{-4}}{2.5 \cdot 10^{-5}} \; 10^2 \tag{2.8}$$

shows that a laminar flow assumption for the flow inside the combustion chamber is sufficient because flow velocities are in the order of 10^0 to 10^1. Close to the gap flow velocities rise to orders of $10^3 m/s$ to $10^4 m/s$ and the flow can turn turbulent. On the other hand, there are two important time scales after the flow chokes. The convection time scale gives an idea on how much time is needed for the flow with velocity U to pass the distance D from close to the gap to the outlet

$$t_{convection} \sim \frac{D}{U} \sim \frac{10^{-3}}{10^2} \; 10^{-5} \tag{2.9}$$

The viscous dissipation time gives an estimation on how long is needed for viscous

Boundary	Pressure [bar]	Temperature [K]	(U_x, U_y, U_z) [m/s]
Inlet	$p_t = 2.1$	$T_t = 400 - 2000$	*pressureInletOutletVelocity*
Outlet	$p = 1$	*zeroGradient*	*zeroGradient*
Walls	*zeroGradient*	*zeroGradient*	*pressureInletOutletVelocity*
Symmetry	*symmetry*	*symmetry*	*symmetry*

Table 2.2: Boundary Conditions

effects at the walls to be transported within the flow area's hydraulic diameter h

$$t_{viscous} \sim \frac{h^2}{\nu} \sim \frac{10^{-8}}{10^{-5}}\ 10^{-3} \tag{2.10}$$

Thus the ratio between convection and viscous dissipation time is

$$\frac{t_{convection}}{t_{viscous}} \sim \frac{10^{-5}}{10^{-3}}\ 10^{-2} \tag{2.11}$$

This means that even if turbulence is created at the walls when the flow is almost choked, the time needed for turbulence to develop inside the flow field is much larger than the residence time of the flow inside the domain. With this scaling assumption the flow can be safely modeled as laminar to save large amounts of computational resources.

2.1.7 Governing equations and solution method

Generally 4 equations are needed to solve for the 4 unknown variables p, T, ρ and U in a compressible calculation. As with most solvers, the solver $rhoSimplecFoam$, which is used here, uses the steady state continuity equation

$$\nabla \cdot (\rho \vec{U}) = 0, \tag{2.12}$$

the steady-state momentum equation neglecting field forces

$$\rho \vec{U} \cdot \nabla \vec{U} = -\nabla p + \nabla \cdot \boldsymbol{\tau}, \tag{2.13}$$

the steady state energy equation in enthalpy form without field forces or sources within the fluid

$$\rho \vec{U} \cdot \nabla (h + \frac{\vec{U}^2}{2}) = -\nabla \cdot \vec{q} + \nabla \cdot (\boldsymbol{\tau} \vec{U}) \tag{2.14}$$

and the ideal gas law

$$p = \rho R T = \frac{\rho}{\psi} \tag{2.15}$$

where ψ is commonly in OpenFOAM defined as

$$\psi = \frac{\partial \rho}{\partial p} \tag{2.16}$$

Source terms are neglected throughout the equations because they are accounted for in the boundary conditions.

Assuming Newtonian Fluid, the momentum equation can be discretized to

$$U_i = \frac{H_i}{a_p} - \frac{1}{a_p}\nabla_i p \tag{2.17}$$

as shown by Jasak [3], who also defines the quantities H and a_p as matrix decompositions from intermediate steps. For better legibility the indices i will be omitted in discretized equations in further equations.

Combining 2.12, 2.17 and 2.15 yields the steady state pressure equation

$$\nabla \cdot \left(\psi p \frac{H}{a_p}\right) - \Delta \left(\frac{\rho p}{a_p}\right) = 0 \tag{2.18}$$

which is the core of the used *rhoSimpleFoam* solver. Its *SIMPLE* algorithm is implemented in OpenFOAM as follows:

1. Initialize, read or create density, pressure, enthalpy, ψ, velocity and flux fields
2. Guess the velocity field U from solving the momentum equation
3. Guess the density using the ideal gas law
4. Set up and solve the pressure equation, repeat for non-orthogonality
5. Update the velocity- and density fields using the newly calculated pressure
6. Solve the energy equation for enthalpy/temperature
7. Repeat until convergence

2.2 Total Temperature Fields

Figure 2-7 shows that the total temperature fields still vary after choking but the errors are around $10\% - 20\%$ and thus much lower than the total temperature changes in *sonicFoam*. A closer look at the flow field in figure 2-8 shows that the errors occur mostly after choking.

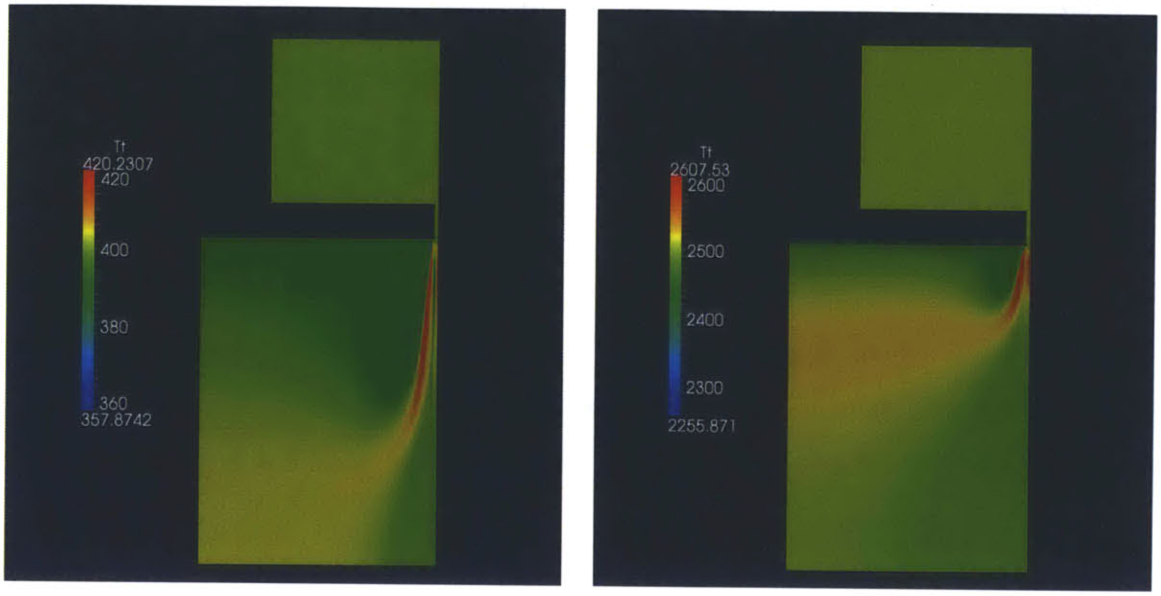

Figure 2-7: Total temperatures for $T = 400K$ (left) and $T = 2500K$

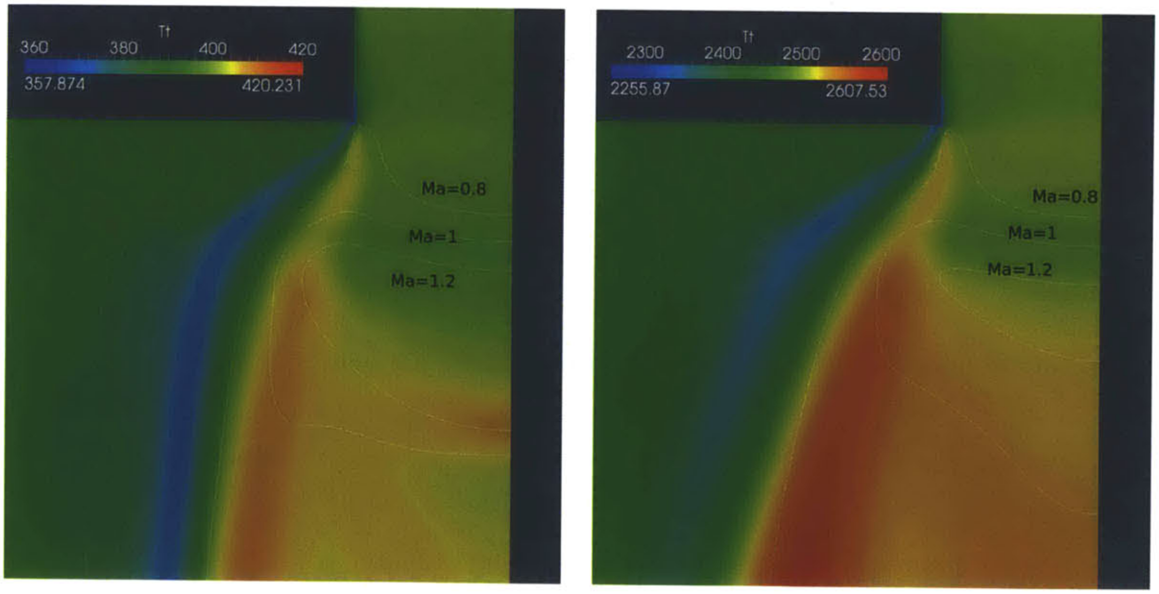

Figure 2-8: Onset of error in T_t for $T = 400K$ (left) and $T = 2500K$

2.3 Blowby flow at the ring gap

Looking directly at the reference area in figure 2-9, two important observations can be made:

1. Boundary Layers decrease the choking area
2. There is only a small section of flow at $Ma = 1$

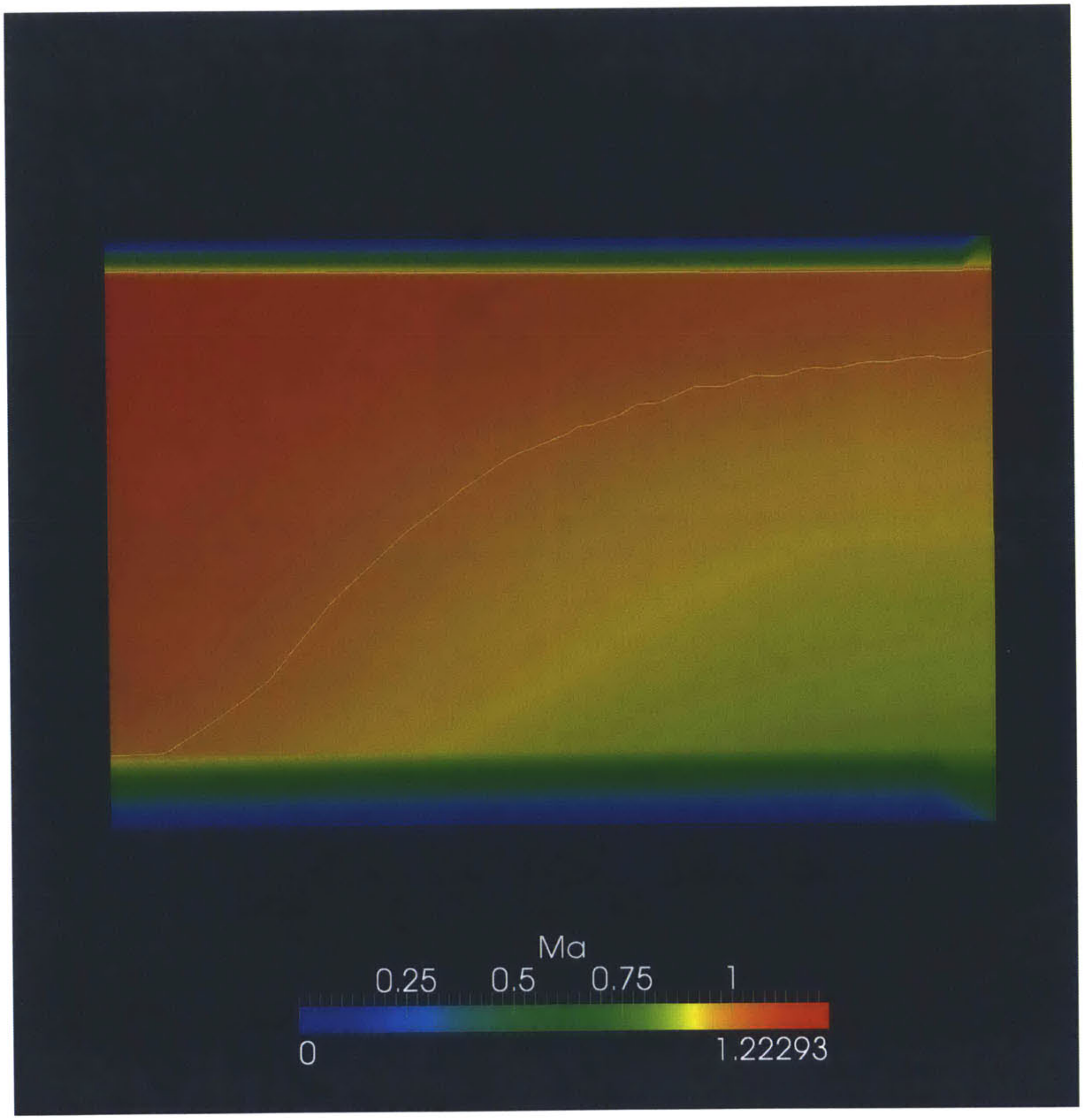

Figure 2-9: Mach numbers inside the Reference Area for $T_t = 400K$

Because the Mach-number varies by around 20% from the expected value of $Ma = 1$ outside the boundary layers, the reference area is not a very good representation of the choking area. The white line in figure 2-9 indicates an isoline for $Ma = 1$ and the large area on the lower right side of the dividing $Ma = 1$ isoline indicates unchoked flow. This implies that the real choking area cannot be represented by any flat two dimensional plane and the reference area is only (part of) a projection of the real choking plane.

Figure 2-11 shows that the flow is choking close to the lower end of the chamfer with the approximate reference area of $A_{ref} = L \cdot d$ which is marked as the black area. As implied by figure 2-9, the real choking area cannot be described in any two dimensional Cartesian room and varies with changes in geometric parameters as in figure 2-10 where contours for $Ma = 1$ are shown inside the computational domain for $C = 0.02$ and $C = 1$. The flow development after the gap and thus the choking area is mainly determined by 3 effects:

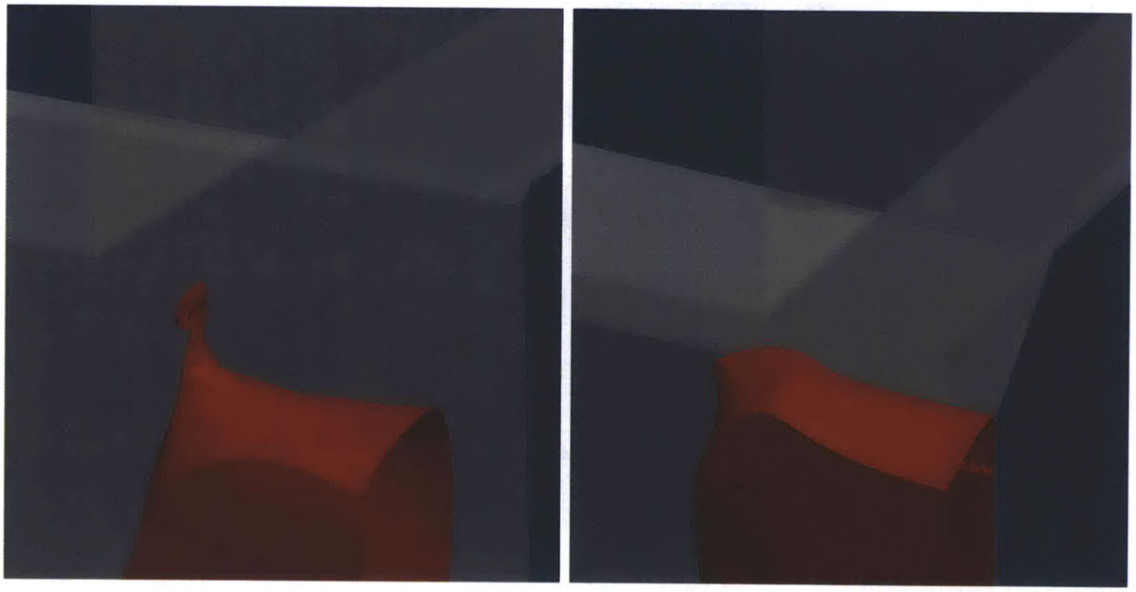

Figure 2-10: Contours of $Ma = 1$ for $C = 0.2$ (left) and $C = 1$

1. Flow area decrease in piston axial direction due to the chamfer
2. Flow expansion into piston circumferential direction due to pressure gradient
3. Flow separation at the chamfer

in addition to the boundary layer effect as shown in figure 2-9.

The first effect can be seen on sketch 2-5 and on the right side of figure 2-11. The left side of figure 2-11 shows a view on the plane normal to the radial piston direction, where we can see the flow expanding into circumferential direction right as it comes out of the ring gap. This effect of flow widening counteracts the decrease in area throughout the chamfer and thus creates a larger choking area than the a priori assumed $A_{ref} = L \cdot d$.

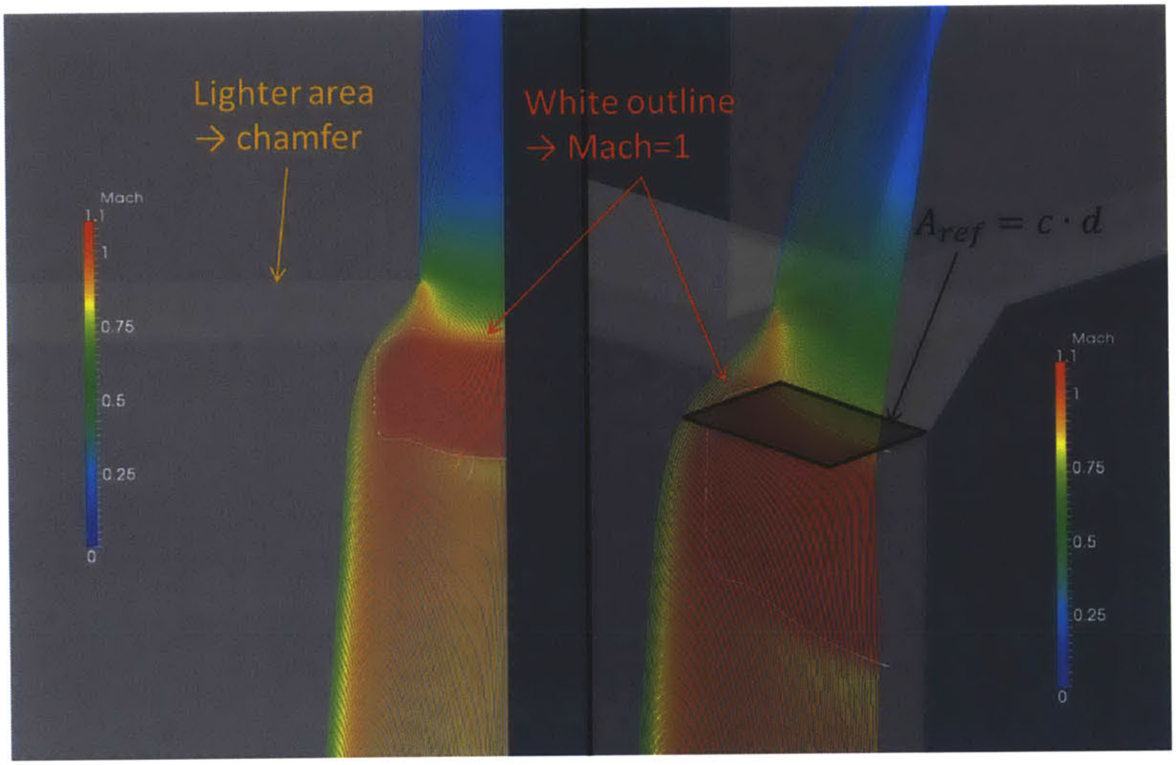

Figure 2-11: Streamlines through the gap

Flow separation at the chamfer can be seen in figure 2-12. If C becomes too small the flow will separate at the chamfer and thus decrease the total flow area.

2.4 Variations of C

The corrected flows per unit areas with the a priori assumed choking area A_{ref} are plotted in figure 2-13. For values of C larger then 0.3 the corrected flow takes a value larger than the theoretical maximum value of 0.57. This indicates that the

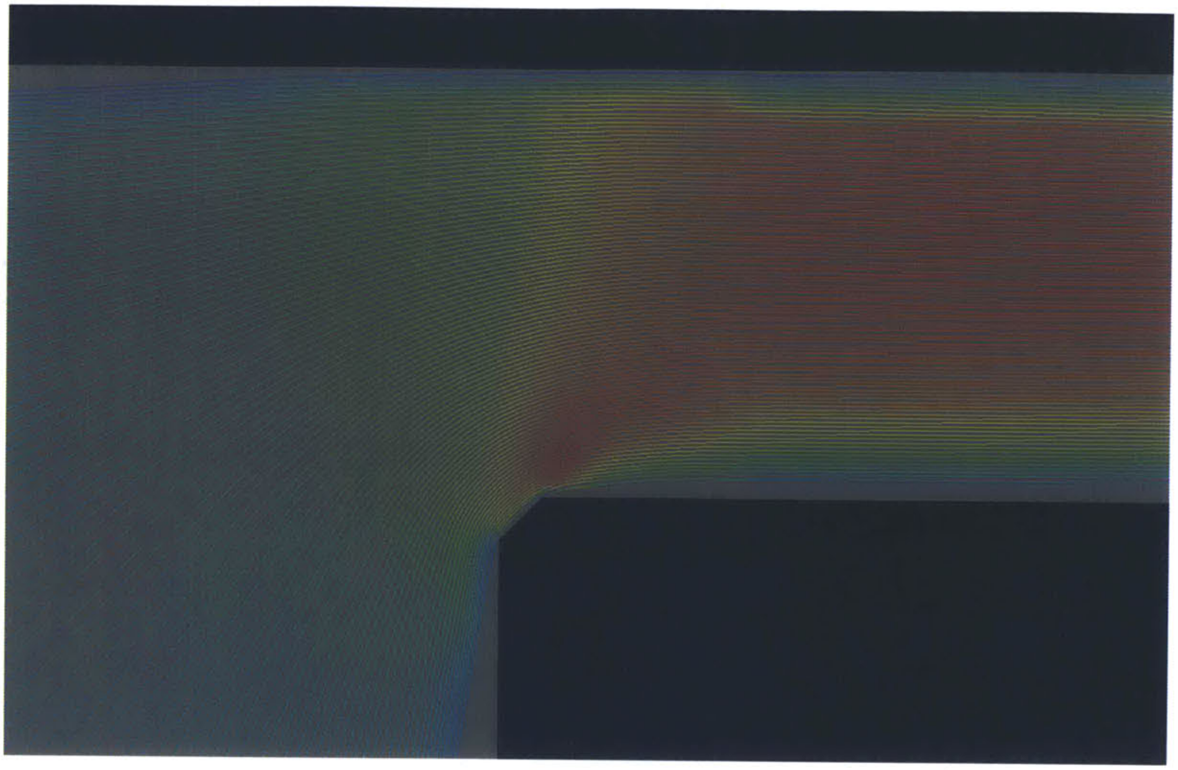

Figure 2-12: Flow separation at the chamfer

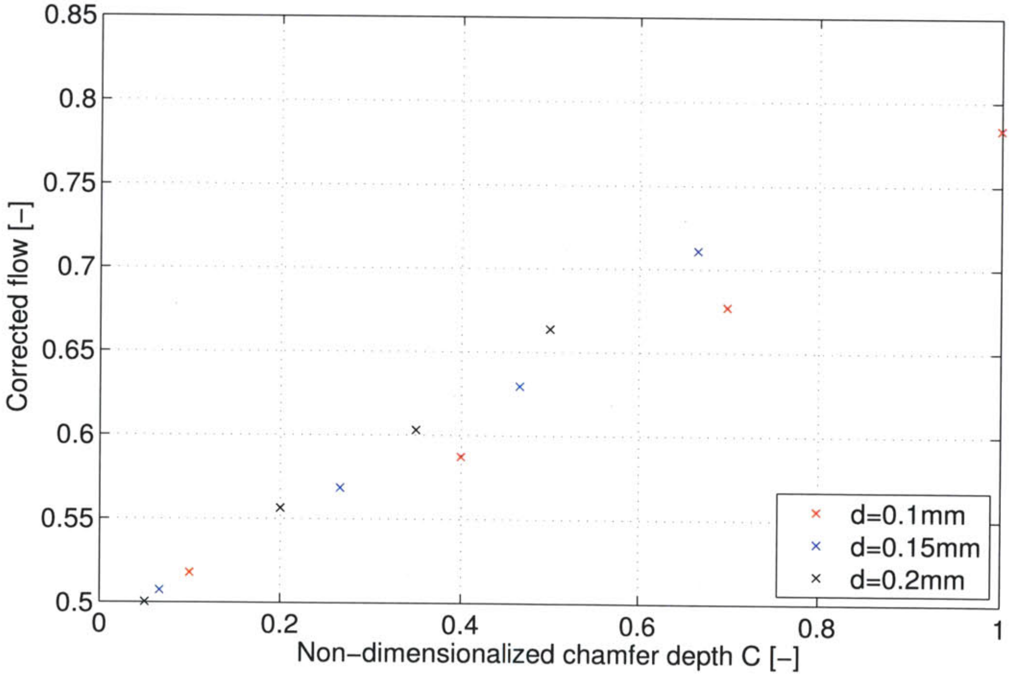

Figure 2-13: Corrected Flow using A_{ref} for different geometries

area used for non-dimensionalization was too small, whereas for values of C smaller than 0.3 the corrected flow indicates a false unchoking of flow, which is due to the non-dimensionalizing area to be too big for that case.

As indicated the flow areas are smaller than the reference area for smaller C where the effect of flow separation at the chamfer is more significant than the flow expansion into circumferential direction. Increasing C keeps the flow better attached to the chamfer by either increase the chamfer length or decreasing the piston-liner distance and thus creating a higher pressure gradient in the radial direction which keeps the flow attached to the piston wall. This results in the flow widening effect gaining more significance over the separation effect and thus effectively increasing the choking area compared to A_{ref}. Rearranging the corrected flow by using its maximum value 0.57 for choked flow yields the real choking areas

$$A_{choking} = \frac{\dot{m}\sqrt{RT_t}}{D_{max} p_t \sqrt{\gamma}} \tag{2.19}$$

The computed areas are non-dimensionalized with the previously assumed reference area A_{ref} and plotted in figure 2-14. This relationship can also be fit linearly for the calculation range and yields the relationship

$$\frac{A_{choking}}{A_{ref}} = 0.51C + 0.85 \tag{2.20}$$

This relationship can be used to non-dimensionalize the mass flows for variations in total temperature which is shown in figure 2-15. As can be seen, the corrected flow per unit area changes very little throughout the study which confirms that the choking area does not change much with variations in stagnation temperature. The main fluctuations in figure 2-15 come from the curve fit approximation.

2.5 Variations of T_t

Because this study focuses on the parametric influence on the mass flow rate, the total temperature can be non-dimensionalized with a reference total temperature which is

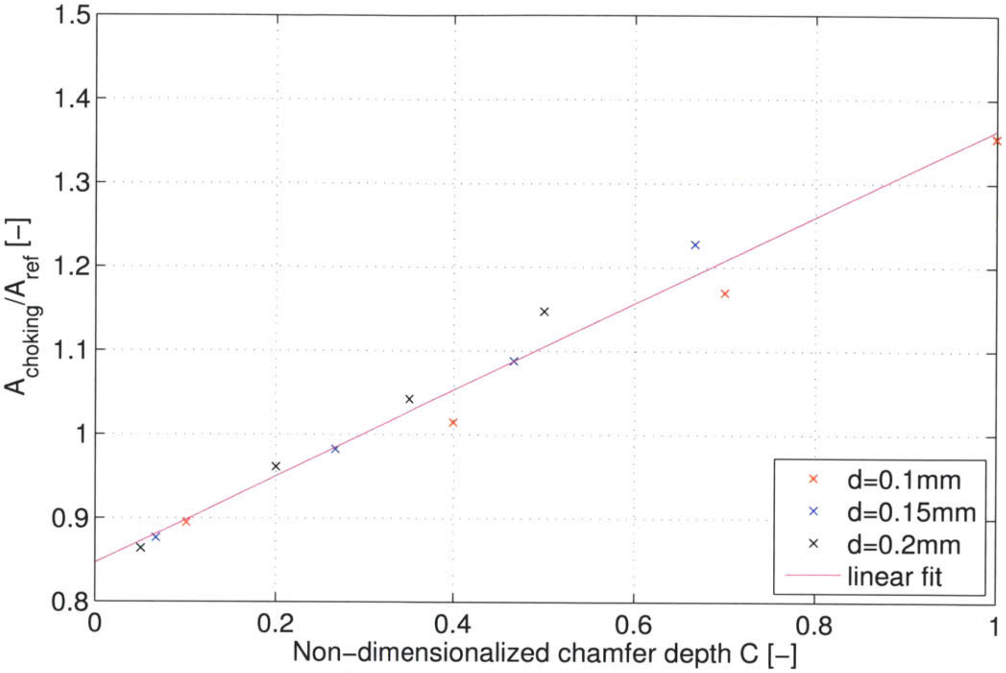

Figure 2-14: Choking Areas

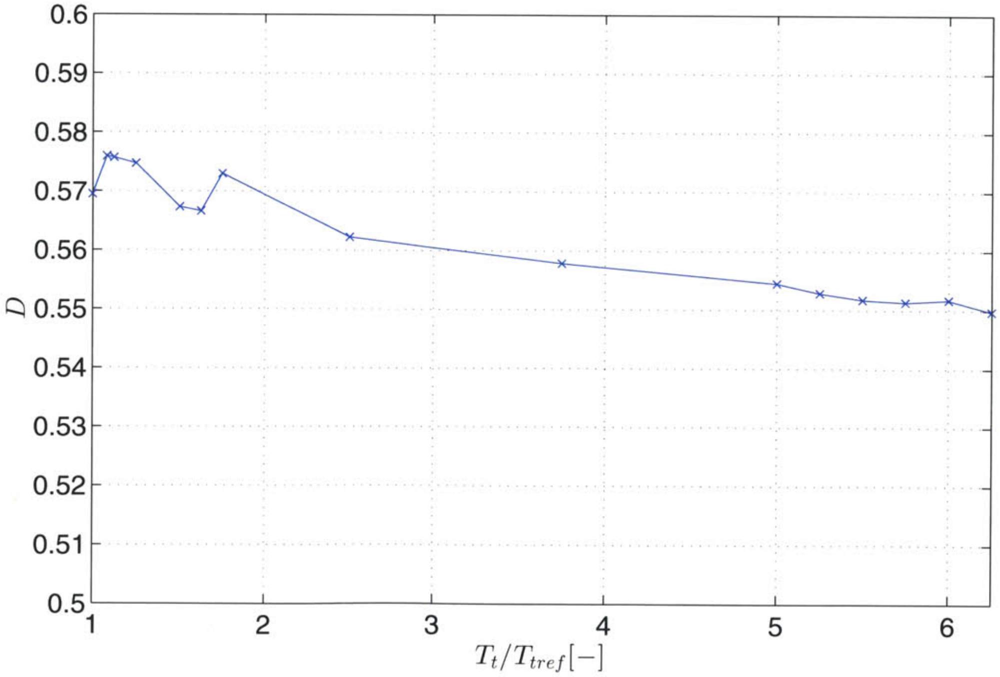

Figure 2-15: Corrected Flow using $A_{choking}$ for different geometries

chosen as the lowest stagnation temperature case of $T_{ref} = 400K$. Similarly the mass flow rate can be non-dimensionalized using the mass flow rate of the reference case with a total temperature of $400K$. Alternatively non-dimensionalizing the mass flow to the corrected flow per unit area is another option, which is more difficult due to the lack of a minimal choking area.

The relationship between absolute mass flow rate and stagnation temperature can be calculated, starting with the absolute mass flow which given as

$$\dot{m} = \rho^* c^* A_{choking} \tag{2.21}$$

where ρ^* and c^* can be calculated with the isentropic flow relationships

$$\frac{\rho}{\rho_t} = \left(1 + \frac{\gamma - 1}{2} Ma^2\right)^{-\dfrac{1}{\gamma - 1}} \tag{2.22}$$

$$c^* = \sqrt{\gamma R T^*} \tag{2.23}$$

$$\frac{T}{T_t} = \left(1 + \frac{\gamma - 1}{2} Ma^2\right)^{-1} \tag{2.24}$$

Plugging in $Ma = 1$ into (2.22) and (2.24) yields

$$\rho^* = \rho_t \left(1 + \frac{\gamma - 1}{2}\right)^{-\dfrac{1}{\gamma - 1}} \tag{2.25}$$

$$c^* = \sqrt{\gamma R T_t \left(1 + \frac{\gamma - 1}{2}\right)^{-1}} \tag{2.26}$$

Plugging (2.25), (2.26) and the ideal gas law

$$\rho_t = \frac{p_t}{R T_t} \tag{2.27}$$

into (2.21) gives the relationship

$$\dot{m} = \frac{p_t}{\sqrt{RT_t}} \left(1 + \frac{\gamma - 1}{2}\right)^{-\frac{\gamma - 3}{2(\gamma - 1)}} \sqrt{\gamma} A_{choking} \tag{2.28}$$

Using the choking area relationship from (2.20) yields the relationship between absolute mass flow and stagnation temperature, which is plotted against calculation values in figure 2-16. This comparison shows good agreement between CFD results and analytically expected values with a maximum error of 6% for the reasonable range of stagnation temperatures.

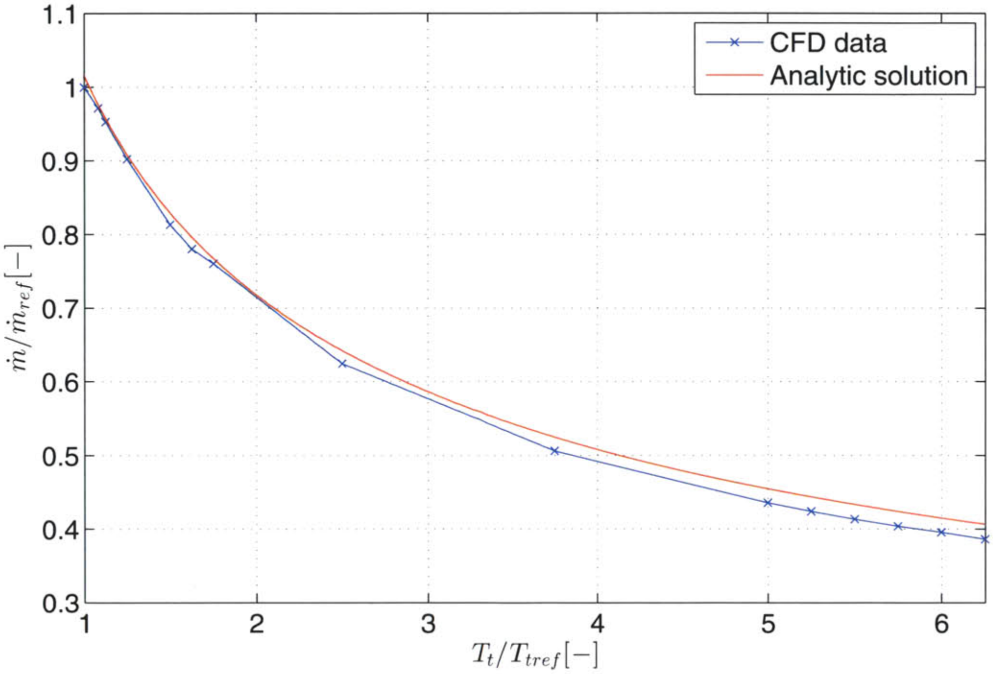

Figure 2-16: Analytical Comparison for Mass Flow Rates

Another interesting observation is the wake behavior that is indicated in figure 2-17. Although the calculation has a 10% error in total temperature in the wake, the qualitative behavior shows that the vortex intensifies and becomes larger as the total temperature is increased. This causes higher mixing losses and results in a faster drop in p_t which causes D to raise and thus unchoke the flow earlier as seen in figure 2-18. Since the geometry does not change in the parametric study for T_t the maximum

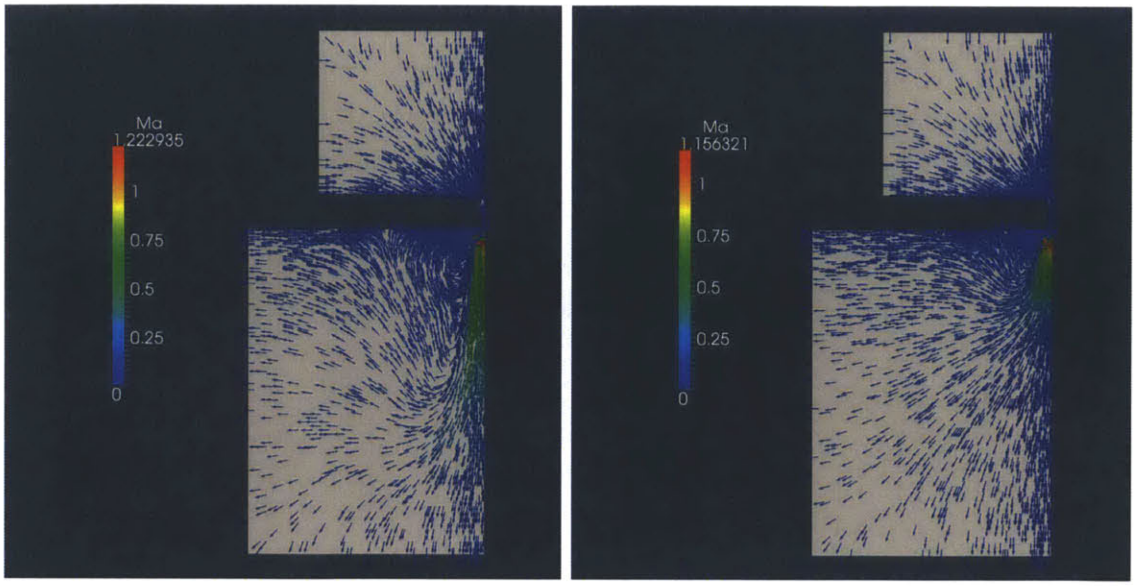

Figure 2-17: Velocity vectors for $T_t = 400K$ (left) and $T_t = 2500K$

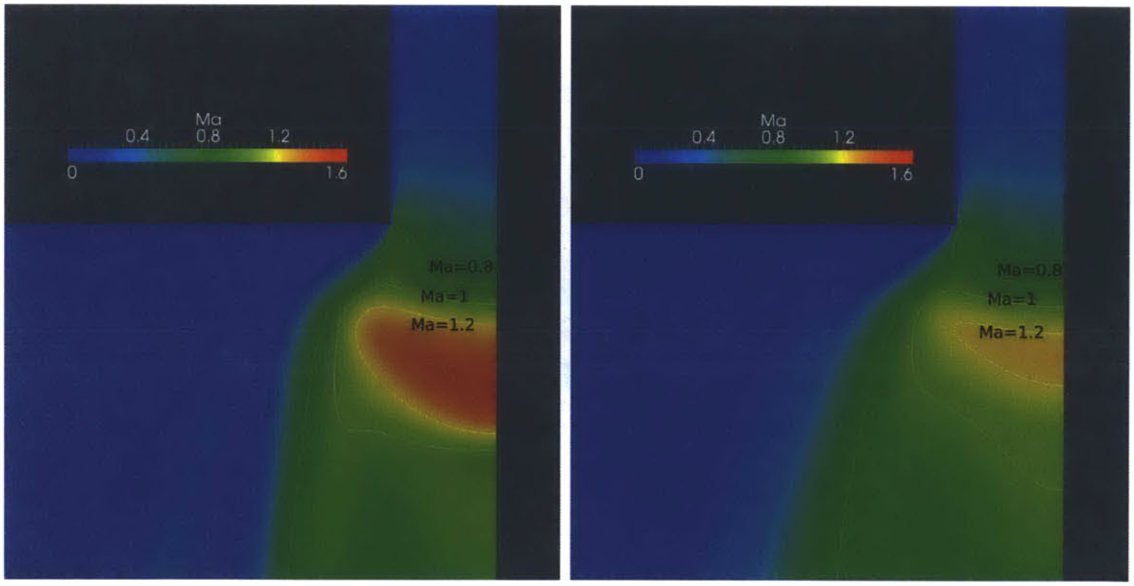

Figure 2-18: Mach numbers for $T_t = 400K$ (left) and $T_t = 2500K$

magnitude of U_x at the boundary layer border is increased while the distance into y-direction remains unchanged, creating a larger velocity gradient and thus larger vorticity, as shown in figure 2-19. Lines with same color refer to velocity profiles at same locations for $T_t = 400K$ and $T_t = 2500K$. Different colors indicate locations of $0.2mm$, $0.3mm$, $0.4mm$ and $0.5mm$ distance from the gap, where higher velocities occur at positions closer to the gap. The exact mechanisc of vortex creation will be

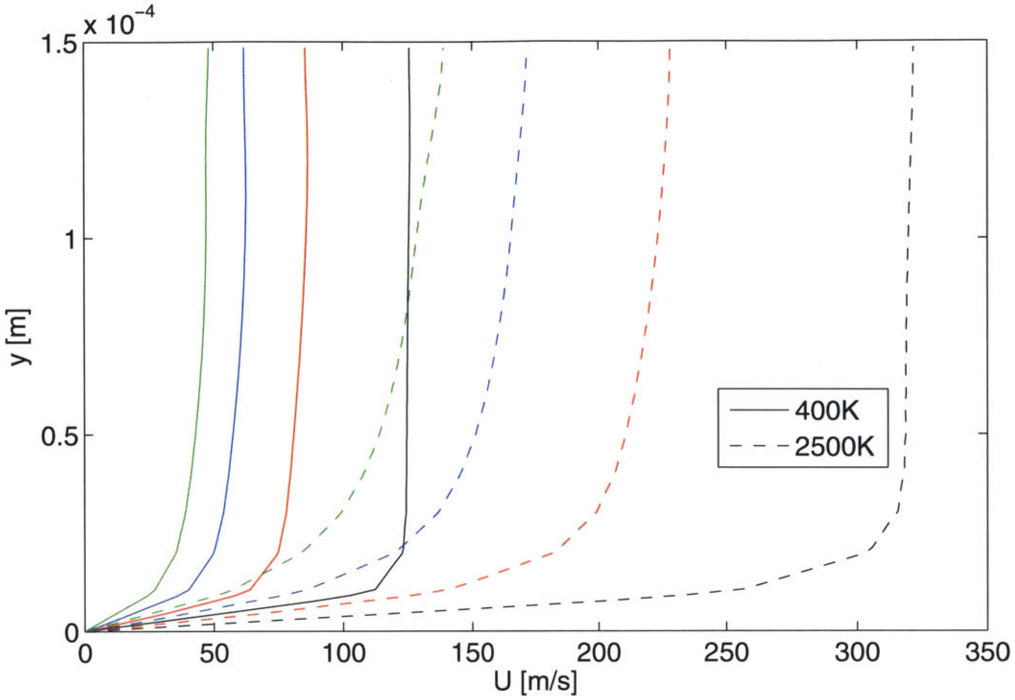

Figure 2-19: Velocity profiles close to the gap

described in more detail in chapter 3.

2.6 Comparison to Previous Results

Tian et al. [11] derived a choking area relationship as

$$A_{choking} = C_D A_{gap} \tag{2.29}$$

where

$$A_{gap} = L\left(d + f \cdot c\right) \tag{2.30}$$

$$C_D = 0.85 - 0.25\left(\frac{p_D}{p_U}\right)^2 \tag{2.31}$$

The chamfer factor f is determined experimentally by industry sponsors and ranges from $0.5-0.7$. Using the given pressure ratio of 2.1 in the calculation gives a discharge coefficient of $C_D = 0.8$. This yields the relationship for the average choking area

$$A_{choking} = 0.8L\,(d + 0.6c) \tag{2.32}$$

The simulated choking area given in (2.20) can be slightly rearranged to

$$A_{choking} = 0.85L\,(d + 0.6c) \tag{2.33}$$

which represents a 6% larger choking area than in experimental measurements. The most likely reason for this discrepancy lies in the omitting of heat transfer during the calculations. As mentioned in figure 2-1 it can be seen that in the subsonic case the corrected flow per unit area is increasing until choking occurs and then decreases again in the supersonic flow region. Heat transfer will raise the total temperature in the flow and will thus increase D and the flow Mach number in the subsonic region, causing the flow to choke earlier at a smaller area. For a more complete calculation heat transfer should be implemented, but there will be additional difficulties in defining a suitable test case because of the non-uniform piston and liner temperatures and the lack of a clear heat transfer area. As seen in figure 2-17, the blowby air is coming from all the groove and combustion chamber. In a real case this air will already be pre-heated to a certain total temperature based on its travel distance before entering the computational domain. Two options to account for the heat transfer inside the combustion chamber are to analytically develop a better total temperature approximation at the boundaries or extending the domain to the full geometry. Neither option is feasible given the resources and time in this work, but could be included in further studies to drive down the 6% error.

2.7 Implications on Oil Transport

Following the discussion of Senzer [8], the amount of oil transport inside the OCR groove can be directly controlled with the amount of blowby. This study shows that the geometric parameters downstream of the gap outlet still play a role in determining the choking area and thus the blowby mass flow rate. Designers can thus focus on ring outlet and chamfer geometries to increase or restrict blowby. Decreasing blowby can be achieved by

- Removing possible chamfers from ring and piston
- Decreasing chamfer size c, piston-land clearance d or gap size L
- Change chamfer angle to choke earlier, giving less time for circumferential expansion and thus decreasing choking area
- Sharpen corners to facilitate flow separation

The implications for oil transport that are gained in the studying of blowby are

- Higher combustion temperatures lead to larger oil accumulation areas below the gap
- Oil from the combustion chamber is more likely to be convected by air flow to the second ring groove if the combustion temperature is lower
- Mixing losses increase as stagnation temperature rises, possibly unchoking the first gap for very high combustion temperatures which would cause an even larger decrease in blowby mass flow
- Smoother flow without separation lead to less areas with no flow and thus less places where oil can sit without being convected by air. Separation and vortices cause oil puddles to form

Chapter 3

2nd land air flow

The main goal in this chapter is to understand where possible oil accumulation areas are and where oil is likely to be convected by blowby. The groove and variations of gap posisions are included to study resulting flow paths and to understand where oil can possibly be transported into and out of the groove.

3.1 Definition of Test Cases

3.1.1 Steady choked condition

The calculations are run in steady state with a choked flow inlet. A first transient calculation is conducted to investigate transient effects, for example gas compression and waves, to understand the time it takes to choke the flow after the critical pressure ratio is achieved. For that purpose, the transient total to static pressure ratio from experimental measurements is imposed as boundary condition. Figure 3-1 shows the pressure ratio and Mach number evolution in time. After a short instable calculation phase of rougly 30 crank angles the Mach number at the inlet follow the same trend as the pressure ratio and hits the choking value 1 only 2 crank agles after the critical pressure ratio of 1.89 is reached. This leads to the conlusion that the choked flow inlet condition is suitable and thus higher pressure ratios will only have an effect on absolute mass flow.

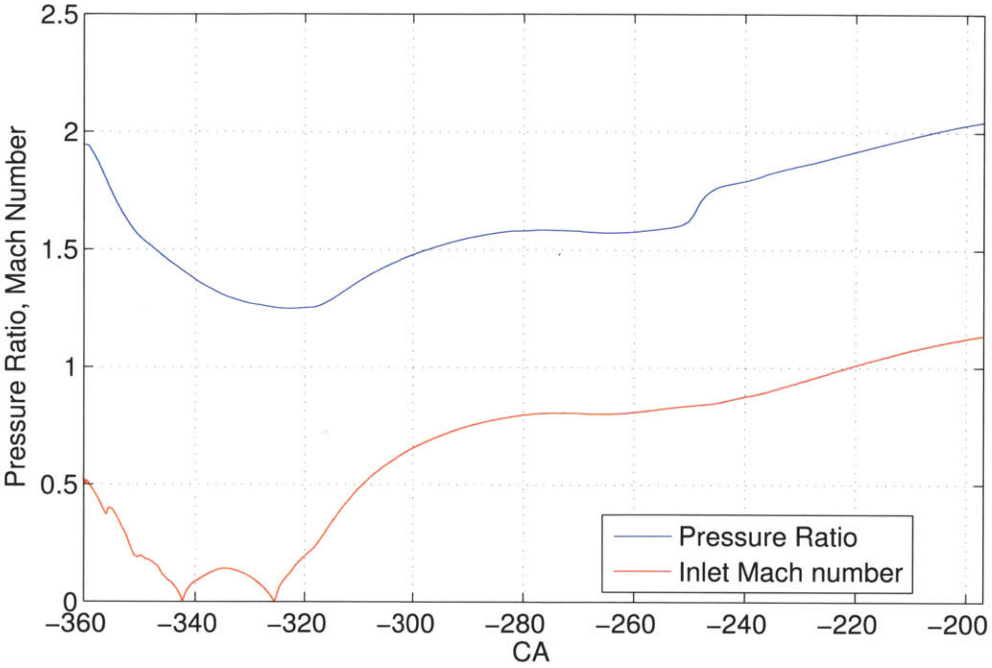

Figure 3-1: Inlet Mach number and pressure ratio

3.1.2 Computational domain

The calculation focuses on the rings being on the lower groove flank conditions, as mentioned in section 1.1.1 with a resulting flow path in the groove as outlined in section 2.1.2. Because the inlet has been determined as choked, a small area in the land's top area can represent the inlet gap. The land itself is either modeled as symmetric half-circle if gaps are exactly opposite or with whole circumferential length for the study of gap positional effects. To reduce exit boundary influences on the flow inside the second land, the computational domain is extended into the third land again using a Neumann type of boundary condition for fully developed flow. Preliminary boundary condition studies showed that velocity waves still existed and influenced the flow pattern at the exit ring gap. For this purpose, the non reflecting exit boundary condition $waveTransmissive$ is chosen, which is described by Poinsot et al. [6]. The resulting symmetric domain is shown in figure 3-2. Non-symmetrical cases vary only the inlet and outlet positions and the inclusion of the other half of the land.

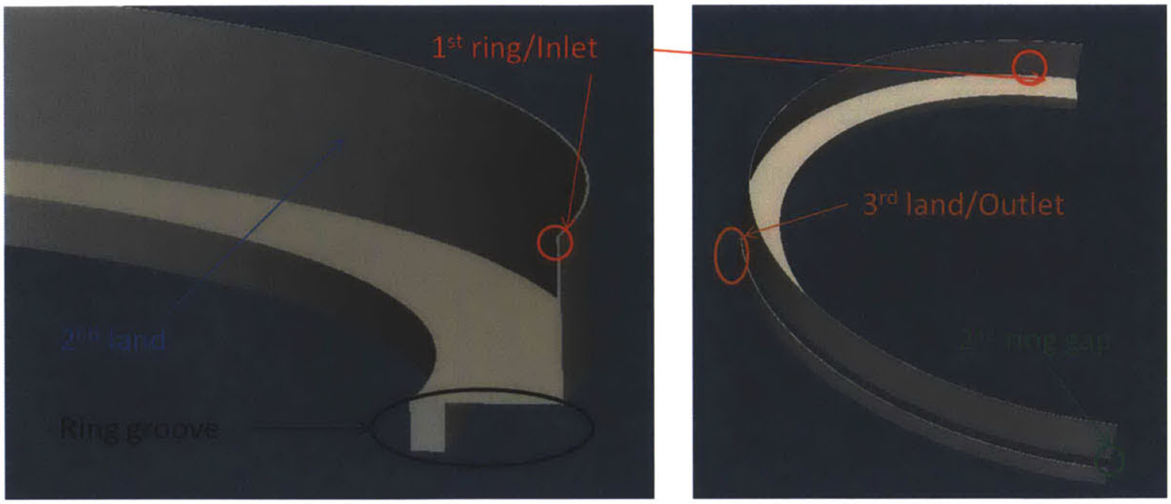

Figure 3-2: Computational domain for land calculations

3.1.3 Boundary conditions

This study uses 4 different boundary types:

- The choked gap inlet is specified by exit static pressure, the measured piston temperature of $T_{inlet} = 423.15K$ and the choked flow velocity which is calculated from $U_{inlet} = c_{inlet} = \sqrt{\gamma R T_{inlet}}$
- The outlet is far away so that Neumann boundary conditions for temperature and velocity hold for the fully developed flow. The pressure is set from experimental measurements for an early compression stroke where static pressures at the inlet and at the outlet are similar. Having a lower back pressure would result in a choking of the third gap as well due to higher losses in the second land. This back pressure effect could be investigated in future studies
- Heat transfer effects are again neglected by the usage of adiabatic walls
- (The whole circular land is split into two symmetrical halfes in the case of exactly opposing gaps)

The boundary conditions for this study are summed up in table 3.1

3.1.4 Governing equations and solution method

The governing equations are the same as outlined in section 2.1.7. For the transient calculation, the only difference are included time derivative terms, which lead to a transient pressure equation of

$$\frac{\partial \psi p}{\partial t} + \nabla \cdot \left(\psi p \frac{H}{a_p} \right) - \Delta \left(\frac{\rho p}{a_p} \right) = 0 \tag{3.1}$$

3.2 Oil accumulation at the inlet gap

The main accumulation area for oil is inside blowby vortices where the low pressure cores can suck and trap oil inside. The intensities and sizes of the vortices vary with total temperature as seen in section 2.5 and can be explained from a vorticity standpoint using a 2D simplification. At the walls before the inlet gap, vorticity is created in the boundary layers and convected with the flow. After passing the sudden expansion, the boundary layer vorticity that is carried by the fluid causes streamline curvature into circumferential direction and thus creates the vortex as sketched on figure 3-3.

For higher stagnation temperatures the amount of vorticity created in the boundary layers increase due to a larger velocity gradient. The z-component of vorticity is defined as

$$\omega_z = \frac{\partial U_y}{\partial x} - \frac{\partial U_x}{\partial y} \tag{3.2}$$

Using the simplified sketch in figure 3-3 assuming parallel flow, the component $\frac{\partial u_y}{\partial x}$ is 0 and the vorticity describes the clockwise rotation rate of the drawn material line. The same conclusion can be achieved from pressure arguments. Because of

Boundary	Pressure [bar]	Temperature [K]	(U_x, U_y, U_z) [m/s]
Inlet	$p = 1$	$T = 423.15$	$(0, -412.34, 0)$
Outlet	$p = 1$	*zeroGradient*	*wavetransmissive*
Walls	*zeroGradient*	*zeroGradient*	$(0, 0, 0)$
Symmetry	*symmetry*	*symmetry*	*symmetry*

Table 3.1: Boundary Conditions

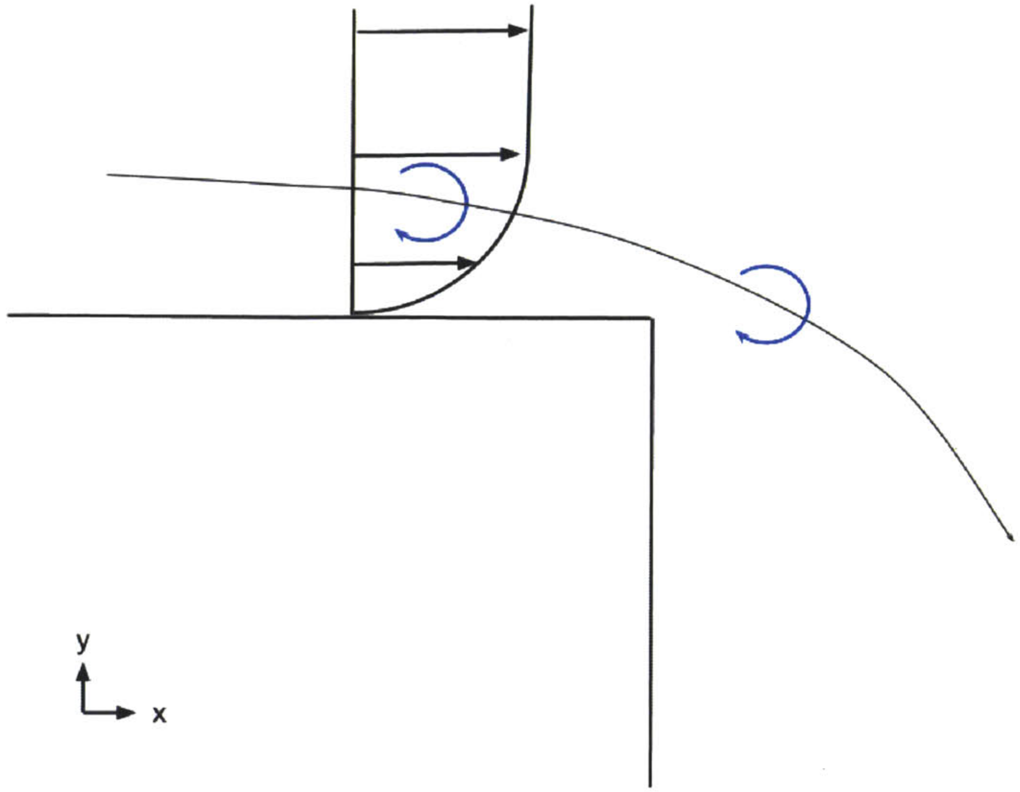

Figure 3-3: Vorticity at sudden expansion

Mach-number similarity throughout variations in total temperature the pressure field is roughly similar based on

$$\frac{p}{p_t} = \left(1 + \frac{\gamma - 1}{2} Ma^2\right)^{-\frac{\gamma}{\gamma - 1}} \tag{3.3}$$

but the velocities inside the groove scale as

$$U \sim c \sim \sqrt{T} \sim \sqrt{T_t} \tag{3.4}$$

For vortices, pressure and velocities follow the relationship

$$\rho \frac{U^2}{r} = \frac{\partial p}{\partial r} \tag{3.5}$$

as outlined by Lord Rayleigh [7]. Having similar pressure fields but larger velocities for higher stagnation temperatures means the vortical radius increases for growing stagnation temperatures.

Another factor on vortex forming that was not included in chapter 2 comes from presence of the second ring. The incoming air stream is slowed down at the second ring wall and creates a stagnation point with high stagnation pressure. This will cause two main pressure gradients to arise:

1. At the second ring, the high stagnation point causes a pressure gradient in circumferential and axial direction pushing the flow away from the stagnation point. This will result in a large vortex inside the land on both sides of the inlet ring gap.
2. Between the ring gap and the stagnation point, expansion causes a pressure drops until the flow unchokes due to mixing losses. These local low pressure regions form smaller vortices, which are unsteady and conveted with the flow. The unsteadyness arises from the asymmetry of the expansion, except in the case where gaps are exactly opposite. Pressure gradients into both circumferential directions are different and thus a tendency towards the higher accelerating direction forces the first secondary vortex into that direction. This leads to a dead space region and subsequent low pressure region on the other side, which will form another vortex and vice versa.

The resulting pressure field and vortices are shown in figure 3-4. There are two main areas where vortices form in a ring down position:

- In the land below the inlet ring gap, as already discussed in chapter 2
- Inside the groove below the the inlet ring gap.

Figure 3-5 shows experimental indicators for the accumulation of oil on both sides below the inlet gap as predicted by the simulated vortices. White areas represent regions of oil accumulation where higher brightness indicates a thicker oil film. Moreover figure 3-6 indicates the unsteady shedding of vortices. One difference in figure 3-6 is

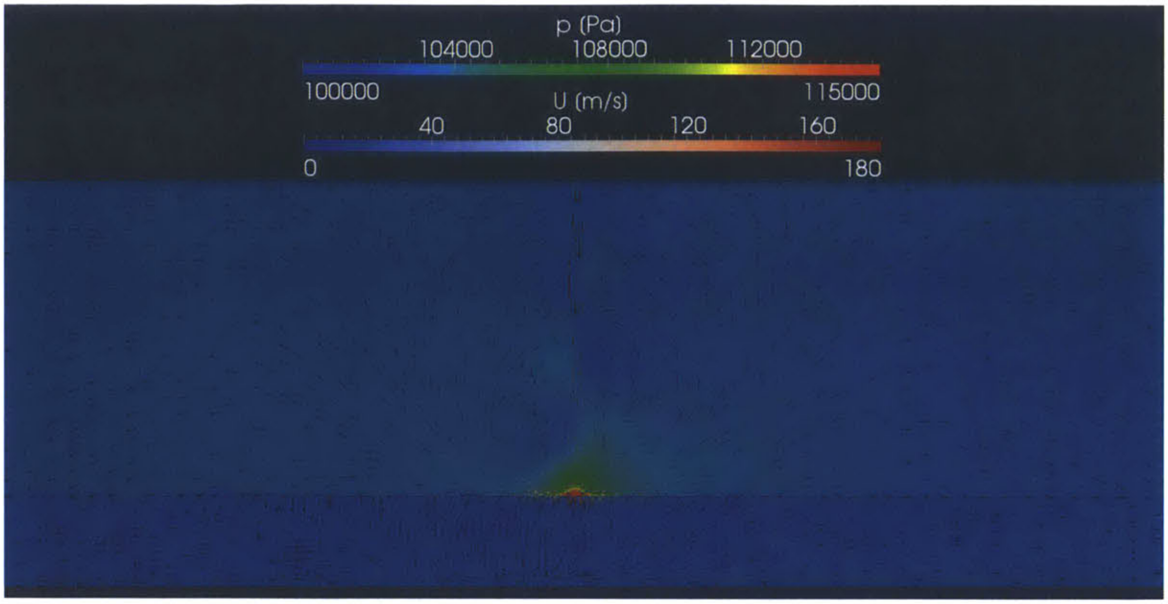

Figure 3-4: Pressure field and velocity vectors below the inlet gap inside the land

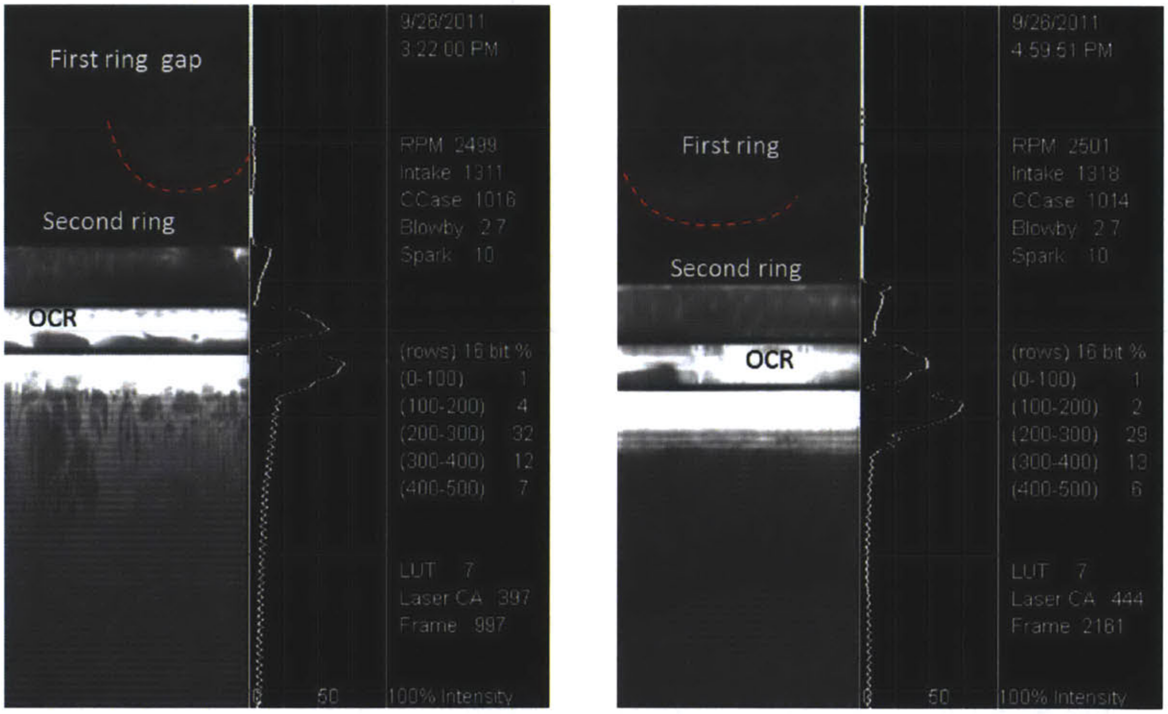

Figure 3-5: Experimental measurement of oil puddles below the first ring gap

the reversed flow direction which implies that the insights gained in this study can be reversed in direction for intake and expansion strokes. After the blowby air reaches the second ring, a part enters the groove due to the high pressure stagnation point on the second ring, as sketched on figure 3-7. The high inertia air flow creates another

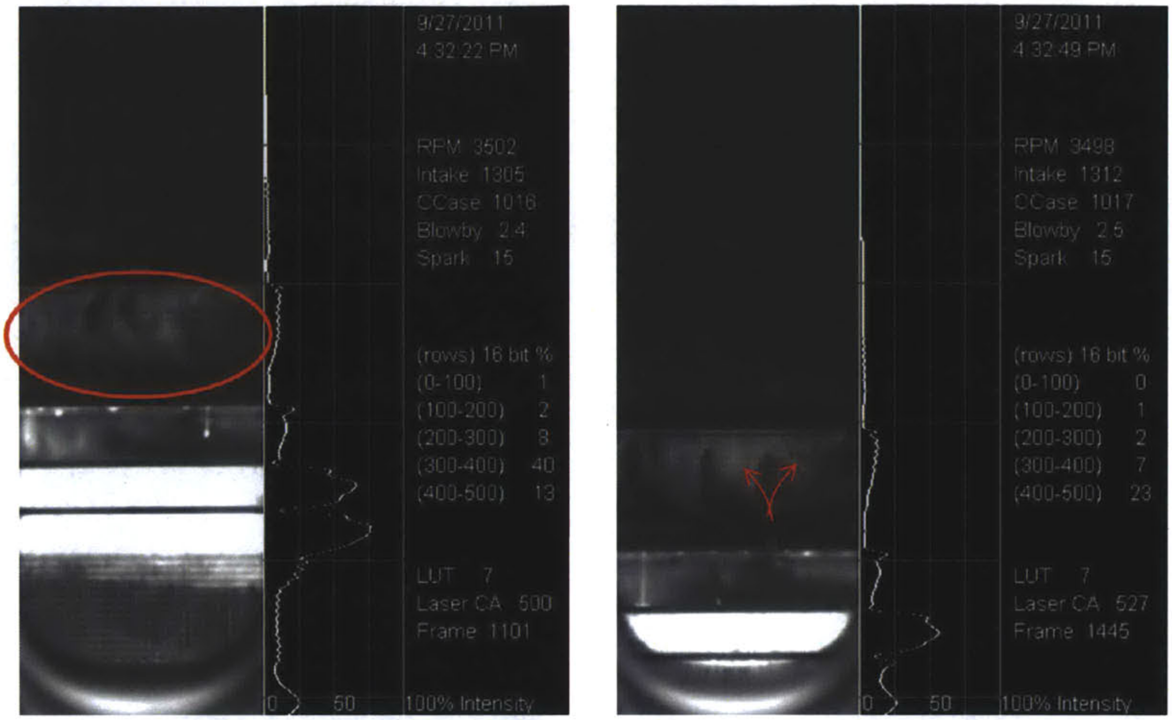

Figure 3-6: Puddle shedding due to unsteady vortices

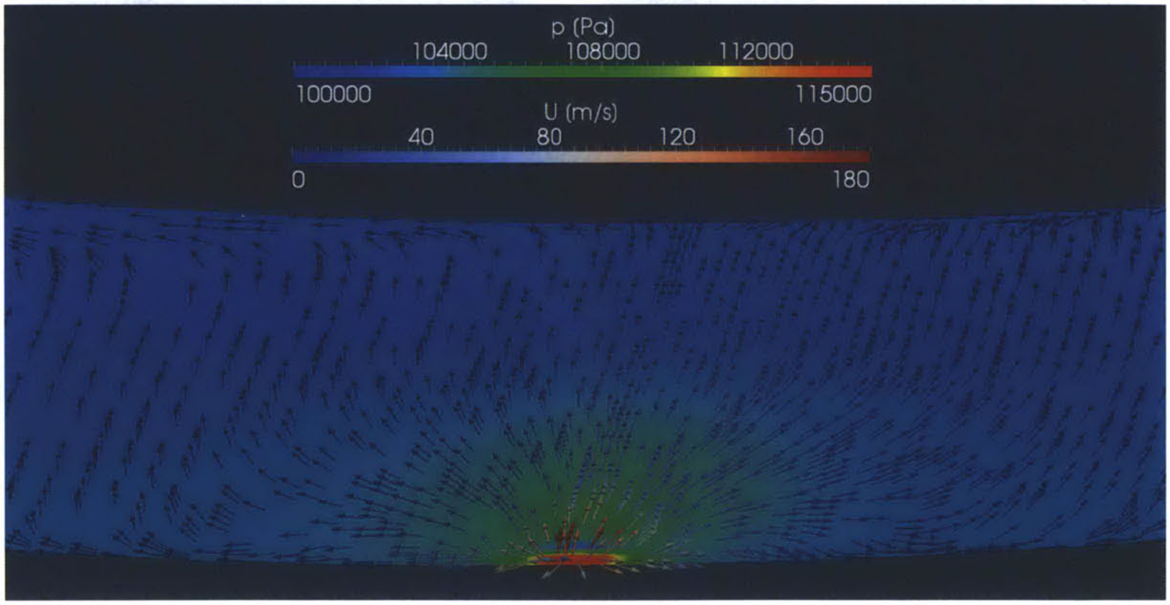

Figure 3-7: Pressure field and velocity vectors below the inlet gap inside the groove flank

vortex in the groove due to the same mechanisms as the vortices below the inlet ring gap, which can be seen in figure 3-8. This causes oil accumulation inside the groove below the ring gap. As oil puddles form within the ring groove, ring movement can

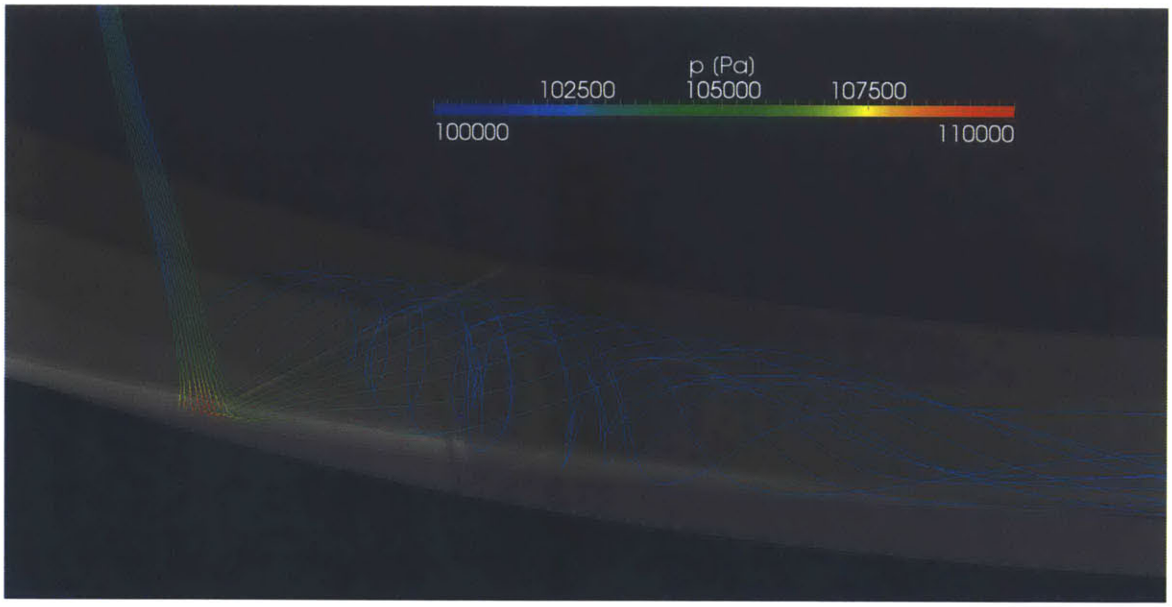

Figure 3-8: Streamlines showing vortices in the second ring groove

push oil out of the groove into the neighboring land, as shown in figure 3-9.

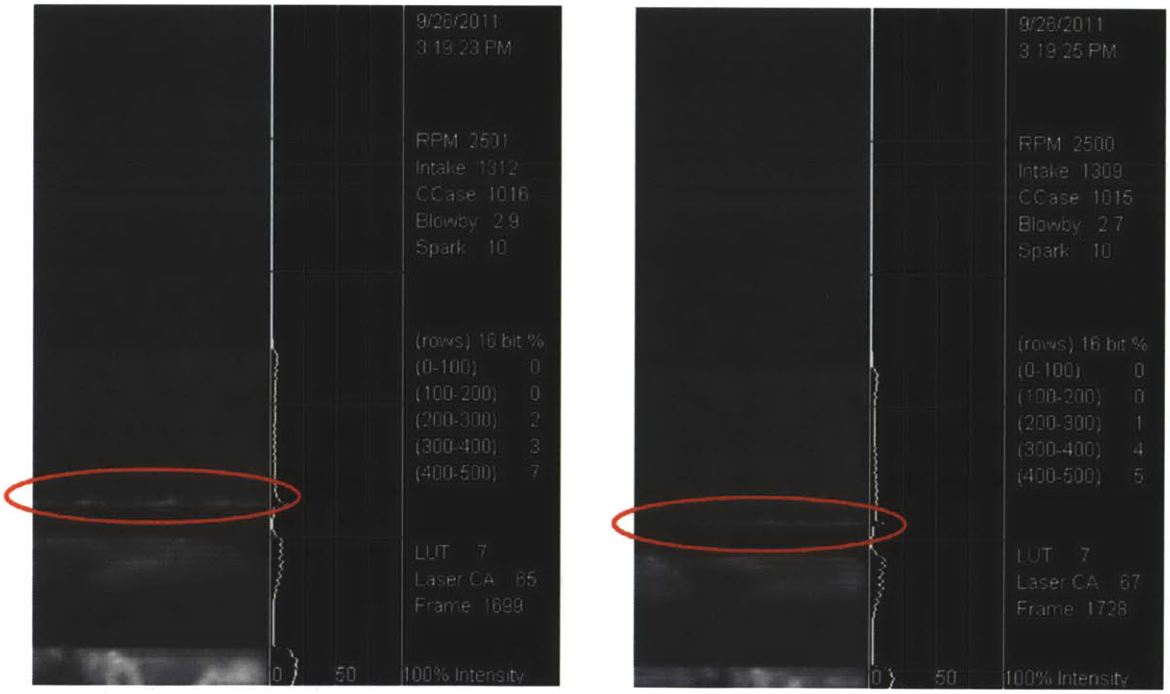

9/26/2011
3 19 23 PM

RPM 2501
Intake 1312
CCase 1016
Blowby 2 9
Spark 10

(rows) 16 bit %
(0-100) 0
(100-200) 0
(200-300) 2
(300-400) 3
(400-500) 7

LUT 7
Laser CA 65
Frame 1699

100% Intensity

9/26/2011
3 19 25 PM

RPM 2500
Intake 1309
CCase 1015
Blowby 2 7
Spark 10

(rows) 16 bit %
(0-100) 0
(100-200) 0
(200-300) 1
(300-400) 4
(400-500) 5

LUT 7
Laser CA 67
Frame 1728

100% Intensity

Figure 3-9: Oil puddles in the crown land, pumped back after accumulatin in first rign groove

3.3 Air flow far away from the gaps

Flow velocities inside the land can be estimated using continuity. Depending on the relative position of the gaps, mass flow from the inlet distributes into both circumferential directions differently. The necessary assumptions area

- The flow inside the lands are laminar, based on a scaling which shows that

  $$Re_D = \frac{UD}{\nu} \sim \frac{10^0 10^{-3}}{10^{-5}} = 10^2 \tag{3.6}$$

  which is clearly below the turbulent onset

- The flow inside the lands is fully developed, which given for the condition that

  $$Re_D \left(\frac{D}{L}\right)^2 \ll 1 \tag{3.7}$$

- The entry length is very short compared to the whole circumference. This can be estimated for laminar flow with

  $$\frac{L_{entry}}{L} = 0.06 Re_D \left(\frac{D}{L}\right) \sim 10^{-2} \cdot 10^2 \left(\frac{10^{-3}}{10^{-1}}\right) = 10^{-2} \tag{3.8}$$

  as outlined by Kundu [4].

This simplifies the Navier-Stokes equation in circumferential direction to

$$0 = \mu \frac{\partial^2 U_{theta}}{\partial r^2} - \frac{\partial p}{\partial \theta} \tag{3.9}$$

Solving the resulting Poiseuille type of flow yields a proportional relationship between velocity in the lands and the pressure gradient. The ratio of flow into the close direction, which is the circumferential direction into which the distance between inlet and outlet gap is shorter, and flow into the far direction M thus scale directly with the ratio of their pressure gradients.

$$M = \frac{\dot{m}_{close}}{\dot{m}_{far}} \sim \frac{\left(\frac{\partial p}{\partial \theta}\right)_{close}}{\left(\frac{\partial p}{\partial \theta}\right)_{far}} \tag{3.10}$$

This can be seen in figure 3-10 where mass flow rates from several calculations with different gap positions are compared to the analytical relationship. The deviation from analytical results as the gaps move closer to each other are due to the shortened time for flow development which causes the fully developed flow assumption to be less accurate.

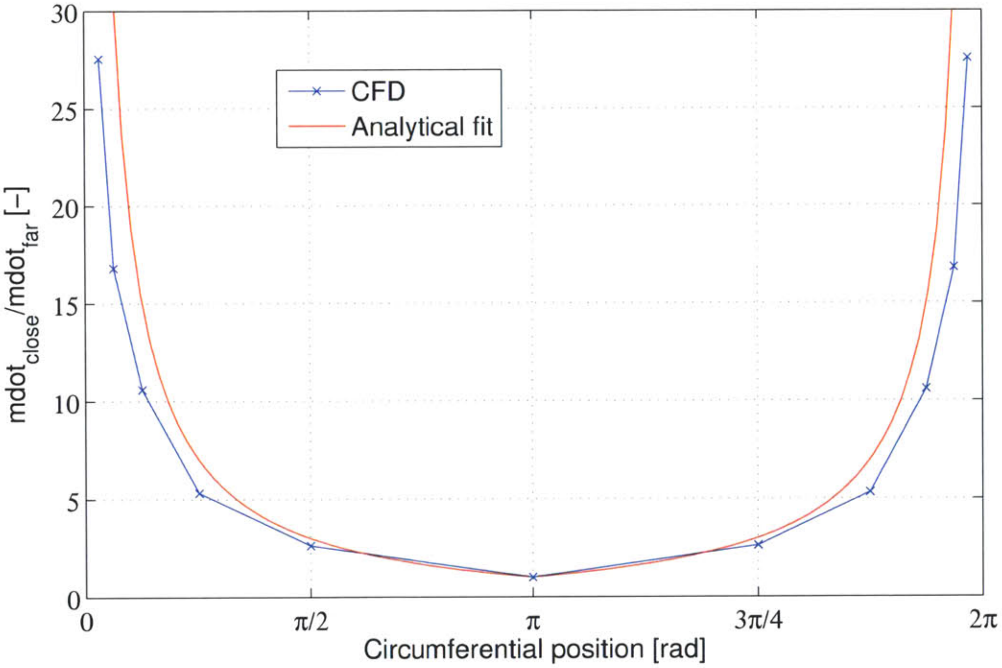

Figure 3-10: Ratio of mass flows for different gap positions

Drawing a control volume as sketched in figure 3-11, where the flow is fully developed at the land border, the mass flow into the close direction is

$$\dot{m}_{close} = \frac{\dot{m}_{close} + \dot{m}_{far}}{1 + \frac{\dot{m}_{far}}{\dot{m}_{close}}} = \frac{\dot{m}_{inlet}}{1 + M} \tag{3.11}$$

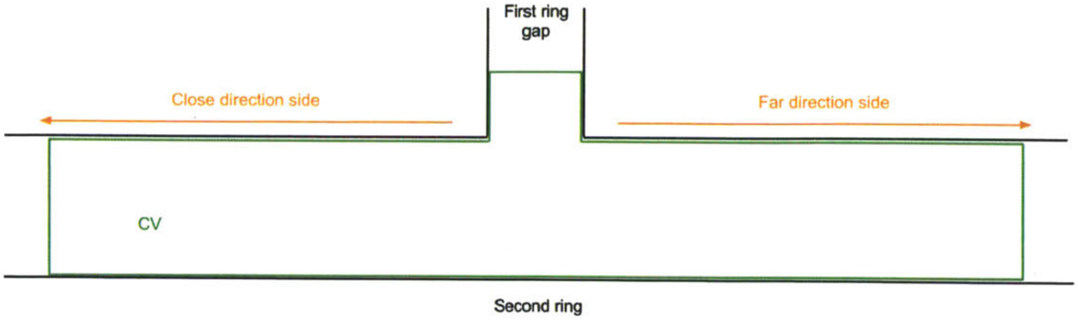

Figure 3-11: Control volume in the second land

The velocity ratio between inlet and close direction outlet can be estimated as

$$\rho_{close} U_{close} A_{close} (1+M) = \rho_{inlet} U_{inlet} A_{inlet} \tag{3.12}$$

which can be rearranged to

$$\frac{U_{close}}{U_{inlet}} = \frac{1}{1+M} \frac{\rho_{inlet}}{\rho_{close}} \frac{A_{inlet}}{A_{close}} \tag{3.13}$$

The density ratio can be estimated using an isentropic flow relationship which slightly underpredicts the value of ρ_{close}

$$\frac{\rho_{inlet}}{\rho_{close}} = \left(\frac{1+\frac{\gamma-1}{2} M_{close}^2}{1+\frac{\gamma-1}{2} M_{inlet}^2} \right)^{\frac{1}{\gamma-1}} \tag{3.14}$$

where the inlet Mach number is 1, giving density ratios $\rho_{inlet}/\rho_{close}$ of 1.36 to 1.58 for Ma_{close} being between 0 and 0.3. The area ratio A_{inlet}/A_{close} is around 0.02. This leads to velocity ratios in the order of

$$\frac{U_{close}}{U_{inlet}} \sim 10^{-2} \tag{3.15}$$

The analysis used a single cross sectional area for the land until now, which can be further divided into land and groove area. In equation 3.9, the pressure gradient is the same in both groove and land but the radial dimension is one order of magnitude larger in the groove than in the lands. Flow velocities in the lands are thus an order of magnitude less than in the groove. The scaling analysis has given two important conclusions about air flow far away from the gaps:

- Flow velocities in the groove are one order of magnitude higher than in the lands
- Flow velocities in the groove are two orders of magnitude lower than at the inlet

This can be seen in the flow cross section on figure 3-12, where the inlet velocity is close to $400m/s$. Comparing the shear forces from the air which scale as $\mu U/h_{flank}$ with the capillary stresses of oil inside the groove which scale as σ/h_{flank} yields the Capillary number

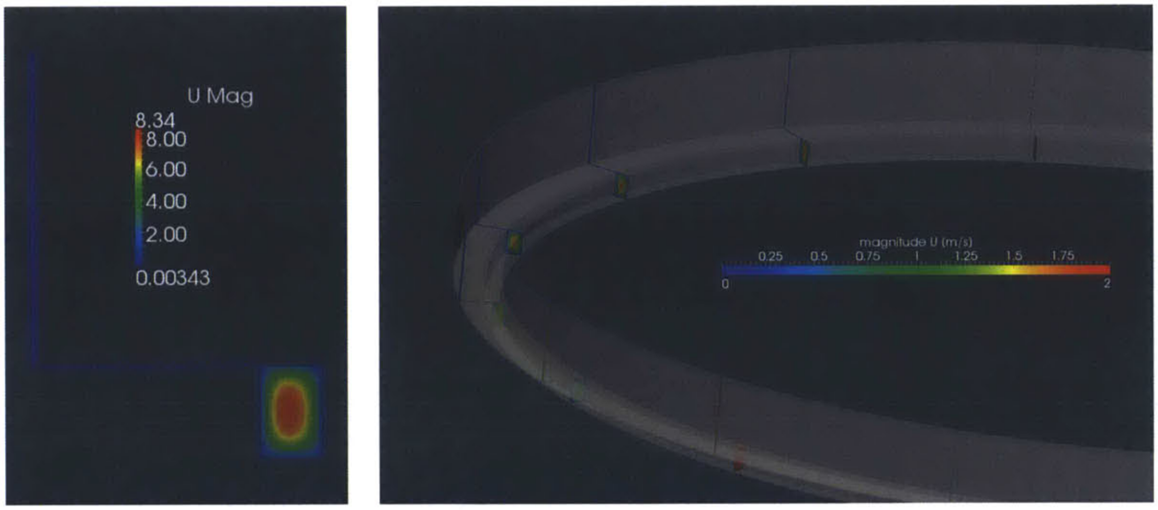

Figure 3-12: Velocity magnitudes in the land and in the groove

$$Ca = \frac{\mu \dfrac{U}{h_{flank}}}{\dfrac{\sigma}{h_{flank}}} = \frac{\mu U}{\sigma} \sim \frac{10^{-5}10^{-2}}{10^{-2}} = 10^{-5} \tag{3.16}$$

The small Capillary number indicates that in most of the land areas, shear effects on oil can be mostly neglected and oil that is far away from either gap is not influenced by airflow into circumferential direction.

3.4 Blowby at the outlet gap

The pressure drop from the upstream influence of the outlet ring gap causes the flow to accelerate. This will cause flow from the land to enter the groove due to its lowered resistance, as mentioned in section 3.2. The extend of upstream influence can be estimated using disturbance theory as outlined by Greitzer et al. [1].

Assuming irrotational incompressible flow upstream up the gap, it can be shown that the upstream influence of the gap pressure disturbance p' satisfies the Laplace equation

$$\Delta p' = \frac{\partial^2 p'}{\partial x^2} + \frac{\partial^2 p'}{\partial y^2} + \frac{\partial^2 p'}{\partial z^2} \tag{3.17}$$

The lack of an intrinsic length scale implies that if a length scale in one direction is set, the length scale in the other directions take the same magnitude. In this case, a length scale set by the geometry is the gap opening. As seen in figure 3-13, only area within one gap opening distance to the gap is influenced by the gap. Because large velocities only occur close to the gap, only oil in the vicinity of the gap will be transported away. This means that it is favorable to have the gap close to areas of large oil accumulation. Examples where this plays a role are

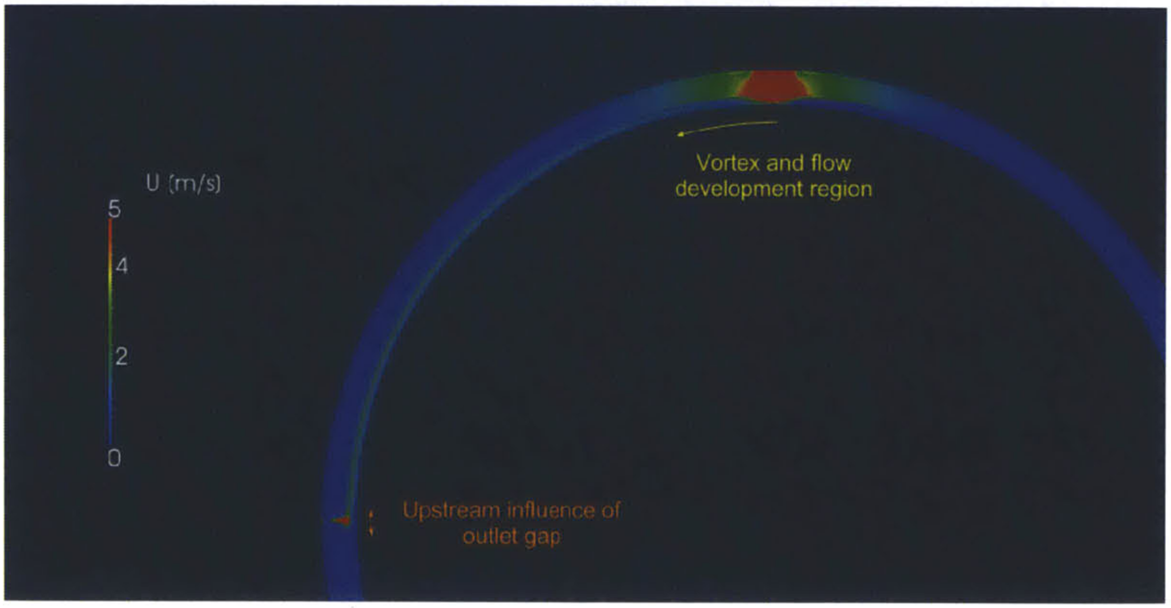

Figure 3-13: Upstream influence of the outlet gap and distance until flow is fully developed

- Large oil puddles from non-conforming oil control rings on the liner
- Leaking areas on the liner
- Oil puddles inside the groove that can be pumped into the second land by the second ring

Equation (3.16) showed that surface tension of oil is dominant compared to shear if velocities are below the order of $10^2 m/s$. This only happens after the upstream influence of the outlet gap has increased flow velocities and thus the dragging of oil only becomes significant at the gap itself.

3.5 Conclusion on 2nd land air flows

The whole flow path is shown in figure 3-14 and the main conclusions for oil transport inside the second land are:

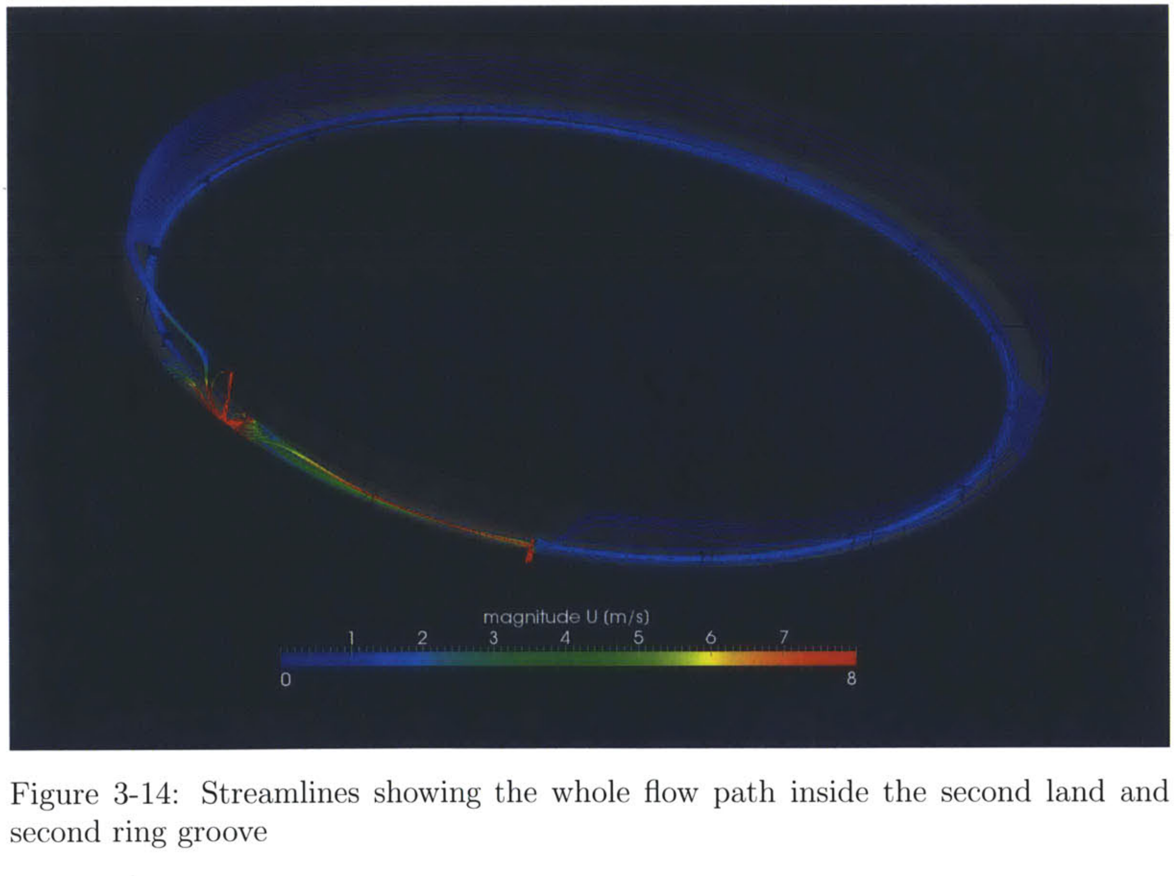

Figure 3-14: Streamlines showing the whole flow path inside the second land and second ring groove

1. Most of the interaction between air and oil happen at the inlet and outlet gap where pressure and velocity magnitudes are up to 20 times as large as in the land section

2. The highest amount of oil accumulation is found at vortices in the land and second ring groove below the inlet gap

3. Transport of oil into groove happens directly beneath the inlet gap due to high land pressure from inlet blowby impact

4. Oil inside the groove will mainly stay and be transported inside the groove due to lower flow resistance in the groove

5. Gap positions determine the amount of air flow rate in each circumferential direction after spreading out into the land based on the pressure gradient

Chapter 4

Multiphase interaction in the 3rd land

Two critical effects in oil transport that happen in the flow cross section in the circumferential lands are the transport of oil into the groove flank, which can then be pumped into the groove and up to higher regions by the rings, and the bridging oil, which can then remain on the liner. Transient multiphase calculations are conducted to understand the different pressure effects at the ring groove entrance and the mechanism of bridging.

4.1 Multiphase solver

The implemented solver *interFoam* uses a typical VOF method where the additional fluid volume fraction variable $\alpha = \frac{V_{fluid}}{V_{air}}$ is introduced, which is used to in this study to visualize oil and air phases for different crank angles.

The standard solver is modified to account for transient body forces as they occur in the piston as shown in Heywood [2]

$$a = -\omega^2 \left(-r\cos t - \frac{r^2(\cos^2 t - \sin^2 t)}{\sqrt{l^2 - r^2 \sin^2 t}} - \frac{r^4 \sin^2 t \cos^2 t}{\left(\sqrt{l^2 - r^2 \sin^2 t}\right)^3} \right) \tag{4.1}$$

where the piston acceleration is multiplied by -1 to account for the acceleration on the fluid.

4.1.1 Governing equations and solution method

The solver uses a PIMPLE algorithm with added equations to solve for the fluid volume fraction and the interface shape. The solver *interFoam* uses the volume fraction transport equation

$$\frac{\partial \alpha}{\partial t} + \nabla \cdot \left(\alpha \vec{U}\right) = 0, \tag{4.2}$$

the incompressible continuity equation

$$\nabla \cdot \vec{U} = 0, \tag{4.3}$$

and the momentum equation

$$\begin{aligned} \frac{\partial \rho \vec{U}}{\partial t} + \rho \vec{U} \cdot \nabla \vec{U} &= -\nabla p + \nabla \cdot \boldsymbol{\tau} + \rho \vec{g} + \sigma \kappa \vec{n} \\ &= -\nabla p_{rgh} - \left(\vec{g} \cdot \vec{x}\right) \nabla \rho + \nabla \cdot \boldsymbol{\tau} + \sigma \kappa \vec{n} \end{aligned} \tag{4.4}$$

where p_{rgh} is the hydrostatic corrected pressure $p_{rgh} = p - \rho \vec{g} \cdot \vec{x}$. Discretizing (4.4) in a similar fashion as (2.13) in chapter 2.1.7 and combining with (4.3) yields the incompressible pressure equation that is used in *interFoam*

$$\Delta \left(\frac{p_{rgh}}{a_p}\right) = \nabla \cdot \left(\frac{H + \sigma \kappa \vec{n} - \left(\vec{g} \cdot \vec{x}\right) \nabla \rho}{a_p}\right) \tag{4.5}$$

The *PIMPLE* algorithm in *interFoam* is implemented in OpenFOAM as follows:

1. Initialize, read or create p_{rgh}, α, velocity and flux fields, average density and viscosity between oil and air
2. Calculate interface curvature , gravity and pressure p
3. Solve (4.2) for an initial guess of α

4. Solve the momentum equation for a velocity predictor
5. Set up and solve the pressure equation, repeat for non-orthogonality
6. Update the velocity- and pressure fields using the newly calculated hydrostatic corrected pressure
7. Repeat until convergence

4.1.2 Interface approximation

A critical parameter for numerical exactness is the mesh resolution. Considering a mesh cell as shown in figure 4-1 the interface curvature κ is approximated as

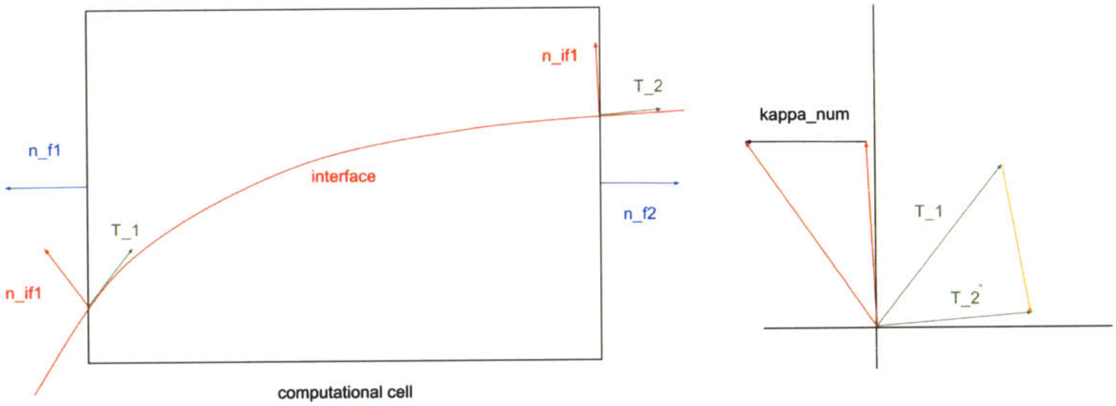

Figure 4-1: Interface approximation used in this study

$$\kappa = \frac{\partial \vec{T}}{\partial s} \approx \frac{(\vec{n}_{if\_left} \cdot \vec{n}_{f\_left})\, dy + (\vec{n}_{if\_right} \cdot \vec{n}_{f\_right})\, dy}{dxdy} \tag{4.6}$$

which is illustrated on the right side of figure 4-1. The main premise for this approximation to be exact enough is that the mesh is fine enough to provide little change in the interface normal vectors at each side of the cell and that $\Delta x \approx \Delta s$. This is especially crucial for large curvature interface areas. A scaling shows the importance of surface effects as

$$We = \frac{\rho U^2 h_{film}}{\sigma} \sim 10^0 \tag{4.7}$$

$$Ca = \frac{\mu U}{\sigma} \sim 10^0 \tag{4.8}$$

for velocities in the order of $10^0 m/s$. This indicates that surface tension effects are around the same order as inertia and viscous effects, so an exact surface reconstruction is necessary for correct results.

4.2 Definition of Test Cases

Two main representative geometries are examined in this study, which are shown in figure 4-2. The simplest design for the second and third ring are flat rings with possible angled ring flanks, where the angle is positive as drawn. Another common design is a hooked second ring with the chamfer on the piston, which is also present in chapter 2.

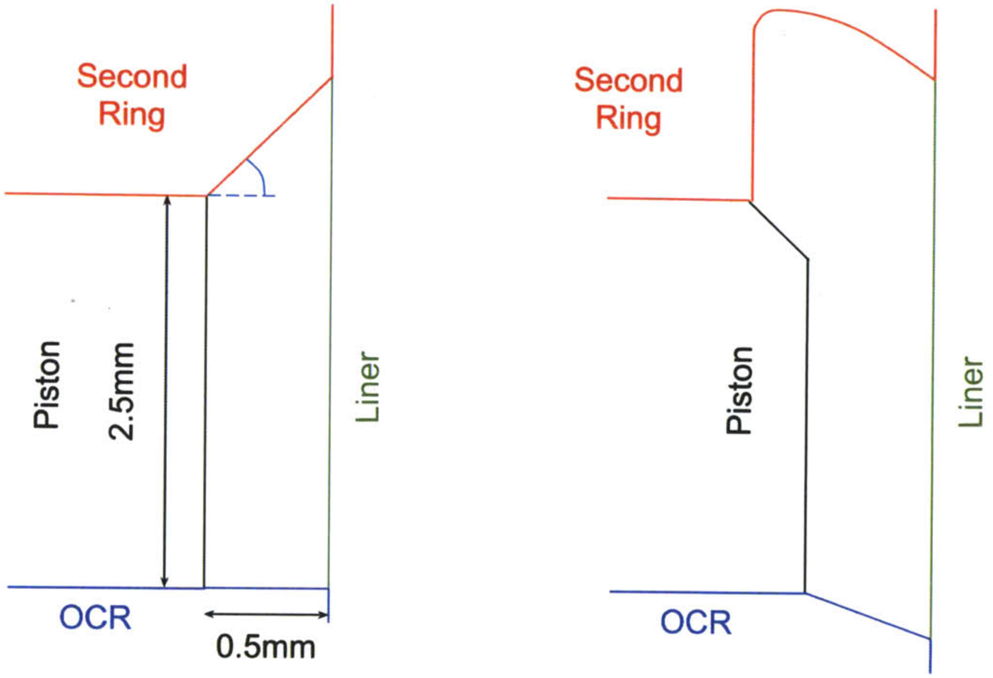

Figure 4-2: Representative geometries for multiphase calculations

This study will focus on the simple 2-dimensional cross sectional case to get a basic understanding of the mechanism at play in the highly unsteady regime, but it is advised to extend the domain to a 3-dimensional case in future studies because of unrealistic bubble behavior and the missing of circumferential distribution, which will flatten out oil puddles.

4.2.1 Computational domain and boundary conditions

The computational domain reflects the 2-dimensional third land in a piston fixed coordinate system, as shown in figure 4-2. In order to capture the piston motion, the piston acceleration is added in as negative body force on the fluid and the negative piston velocity is assigned to the liner.

4.2.2 Mesh resolution

Based on the reasons outlined in section 4.1.2, a mesh study is conducted with 3 different mesh refinement levels called *coarse*, *fine* and *superfine*. A short test is conducted to track the position of an oil drop as shown in figure 4-3. Computational time increases roughly 30-fold between *coarse* and *fine* whereas the computational time increases by 10-fold between *fine* and *superfine*, although the positional differ-

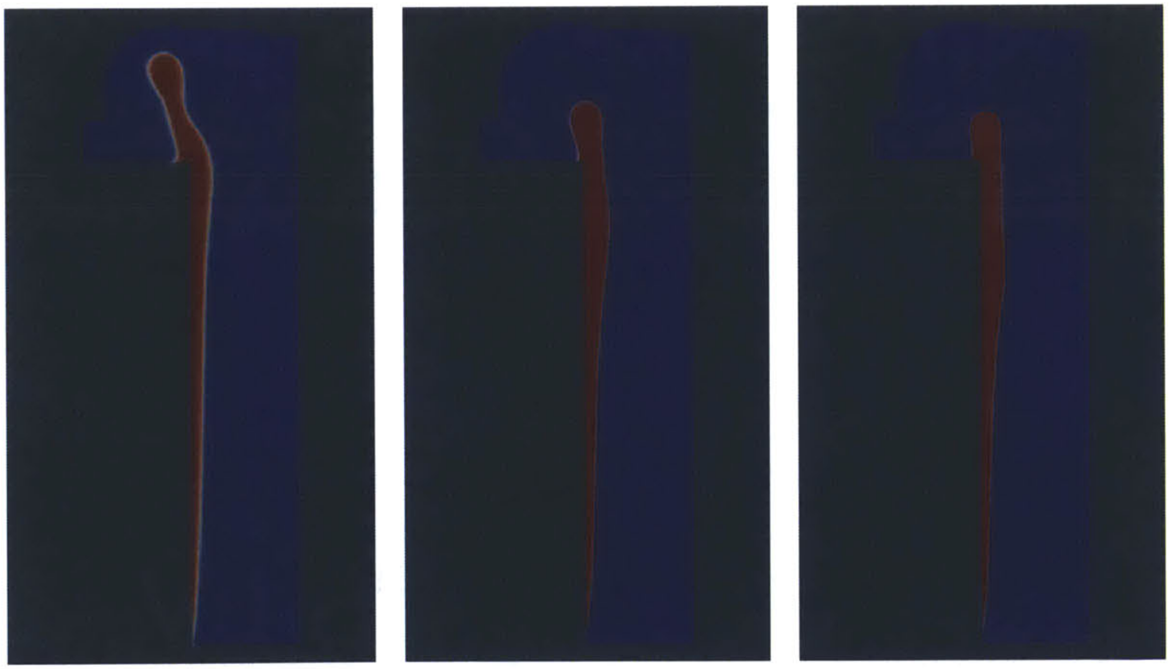

Figure 4-3: Oil drop positions for different mesh refinement levels

ence is less than 1% of the total piston wall heigth between the finer two meshes. For computational resourcefulnes, the *fine* mesh is chosen for all subsequent calculations.

4.3 Pressure effects at the second ring groove inlet

4.3.1 Hooked second ring with rectangular chamfer

Figure 4-4 shows the time evolution of pressure at the ring groove inlet for $3000rpm$ and an oil area to domain area ratio of 0.1 for a hooked second ring with chamfer. The shape indicates a periodic effect between $-250Pa$ and $300Pa$ gauge pressure

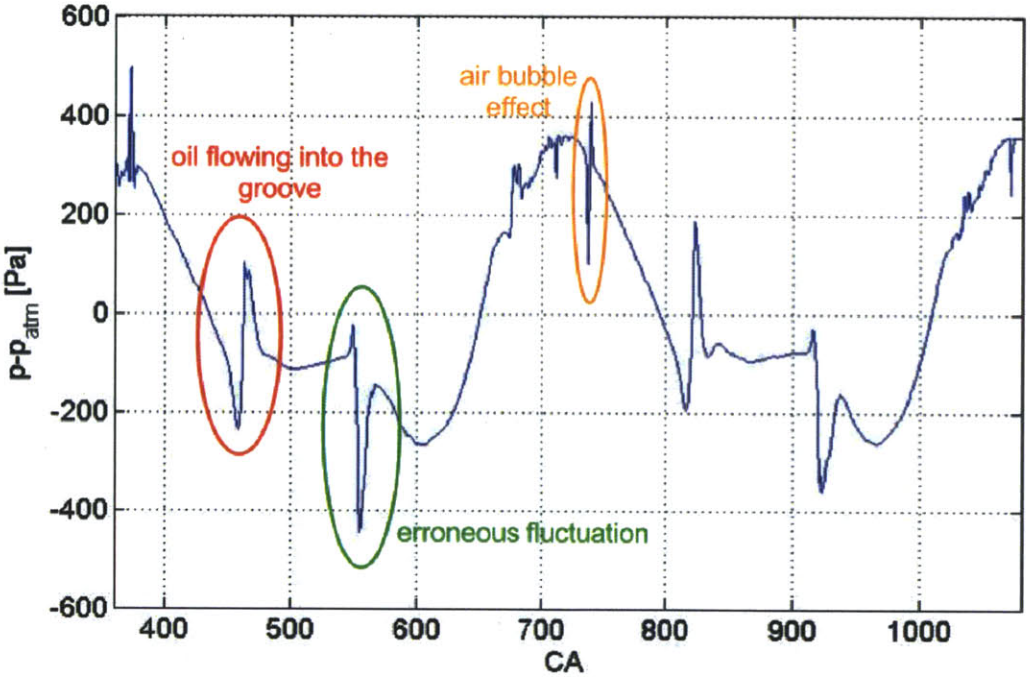

Figure 4-4: Groove inlet pressure at 3000rpm for the hooked ring design

with several small spikes. The effect which are causing this shape are

- hydrostatics
- calculation errors produced by OpenFOAM
- oil flowing into the groove and changing the surface shape as shown in figure 4-5a

- air bubbles at the groove changing the surface shape as shown in figure 4-5b

(a) Oil flowing into the groove

(b) Trapped air bubble

Hydrostatics can be easily calculated as $p_{hyd} = \rho a_{max} h_{chamfer} = 513Pa$ which is the pressure difference between TDC and BDC. Although the other effects pressure effects can be in the same order of magnitude, they almost completely negate themselves due to fluctuating over and under the mean background hydrostatic pressure for the same amount of time. Moreover the duration of half a period is less than 10 crank angles for the small fluctuations which limits their influence on oil transport. This means that for the hooked second ring with rectangular chamfer design, hydrostatics are the main effect in the land to influence oil transport at the groove flank.

For a more complete understanding of oil transport, the capillary effect inside the groove flank must be considered. Comparing the hydrostatic pressure at the inlet to the capillary forces inside the groove flank with a flank height $h_{flank} = 50\mu m$

$$Bo = \frac{\rho a_{max} h_{chamfer}}{\frac{2\sigma}{h_{flank}}} = 0.64 \tag{4.9}$$

shows that capillary forces are one order of magnitude larger than the hydrostatic effect.

The velocity in the groove flank can be described as a fully developed 2 dimensional Poiseuille flow with no slip boundary conditions at the walls at $y = 0$ and $y = h_{flank}$

$$u_{x_{flank}}(y) = \frac{1}{2\mu_{oil}} \frac{\Delta p}{\Delta x} \left(y^2 - h_{flank} y\right) \tag{4.10}$$

The mean velocity is

$$\bar{u}_{flank} = \frac{1}{h_{flank}} \int_0^{h_{flank}} u dy = -\frac{1}{12\mu_{oil}} \frac{\Delta p}{\Delta x} h_{flank}^2 \tag{4.11}$$

With a pressure gradient of $400Pa/(L_{groove}/2)$, the flank velocity is $0.0088m/s$. Non-dimensionalized with a cycle time of $0.02s$ for $3000rpm$ and the groove length of $1.9mm$, the non-dimensionalized velocity

$$v = \frac{\bar{u}T}{L_{groove}} = 0.09 \tag{4.12}$$

which means that 9% of the groove is filled within the time of one cycle. To support the calculated velocity another test case is conducted with an added groove flank channel, as shown in figure 4-5d, compared to the original domain in figure 4-5c. The outlet to the groove is set to atmospheric pressure and connected to a patch on the liner, which represents the pressure exchange between groove and land which would happen in a real 3D case. Figure 4-5 shows the gauge pressure, the velocity and the interface location inside the groove flank centerline for a given crank angle. The jump in alpha from 0 to 1 indicates the interface location and the positional coordinate x starts at the groove flank inlet in the land and ends in the groove. The velocity is slightly above the calculated value because the centerline shows the maximum velocity instead of the mean velocity.

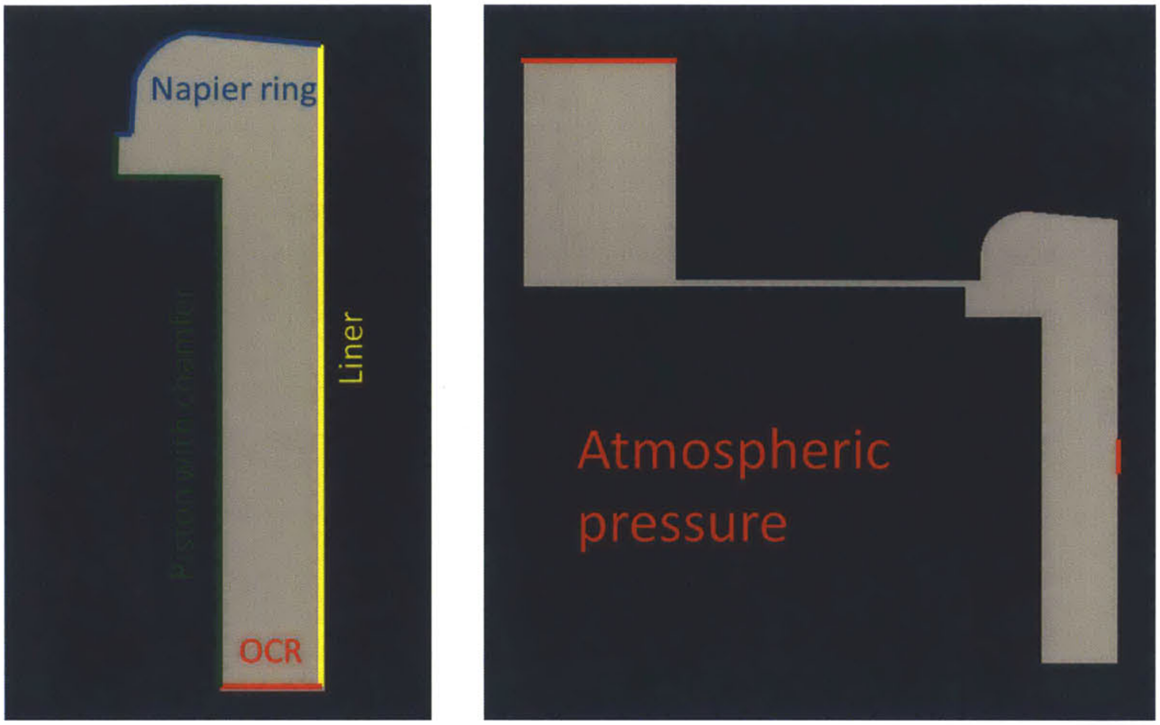

(c) Original domain (d) Extended domain with groove

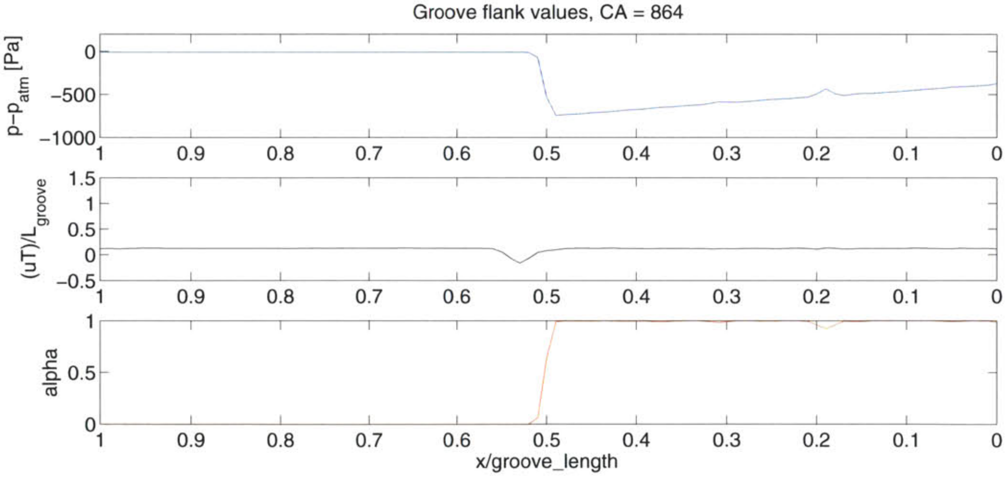

Figure 4-5: Groove flank centerline values at CA=144

4.3.2 Rectangular second ring

Figure 4-6 shows the pressure evolution at the ring groove flank inlet for $3000rpm$ and an oil area to domain area ratio of 0.1 with a flat second ring without chamfer configuration. Main differences from the hooked ring with chamfer setup in this setup are

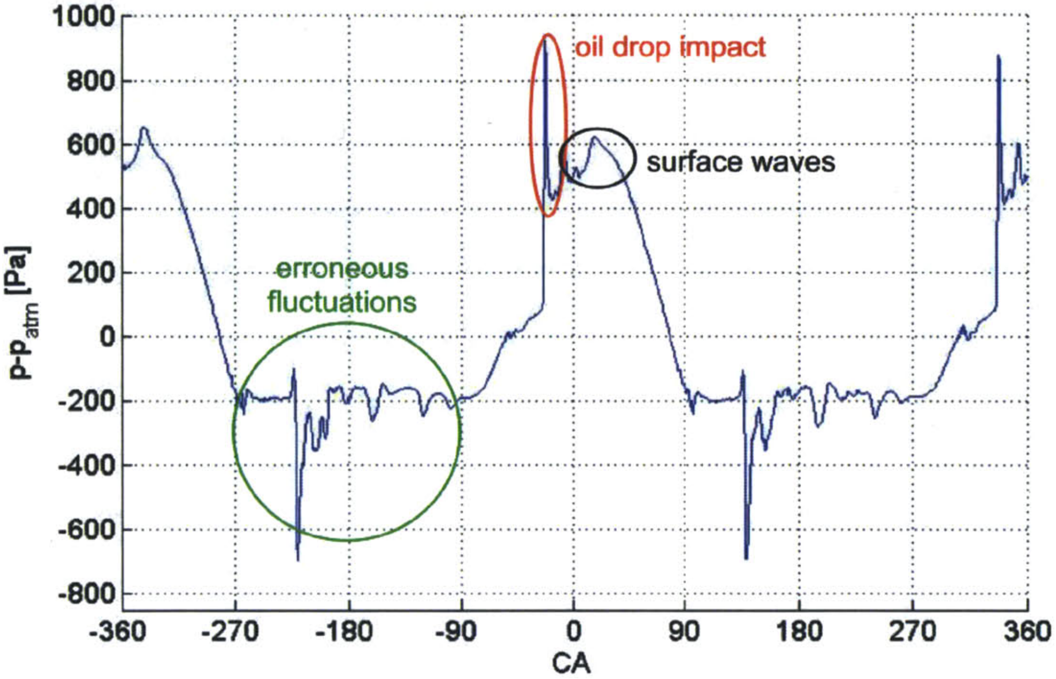

Figure 4-6: Groove inlet pressure at 3000rpm for the rectangular ring design

- changes in the magnitude of hydrostatic pressure
- stagnation pressure effects from traveling oil drops hitting the second ring at the groove flank inlet, as shown in figure 4-7a
- surface wave effects changing the interface curvature and thus modifying the Laplace pressure. Surface waves can occur during early downstroke where oil is still at the second ring and the liner is traveling upwards, dragging oil and air upwards and thus creating vortices, as shown in figure 4-7b

The main driver for pressure fluctuation in this case is again the hydrostatic pressure effect. Interestingly the magnitude of pressure fluctuations due to hydrostatics does not increase for this case, although the possible hydrostatic height is two orders of magnitude higher than in the hooked ring case. The reason lies in the vortex which disconnects the stagnant oil puddle at the ring groove inlet from the remainder of the oil . This means that for looking only at pressure effects at the groove inlet, the difference between both setups is small and the amount of oil pumped into the groove

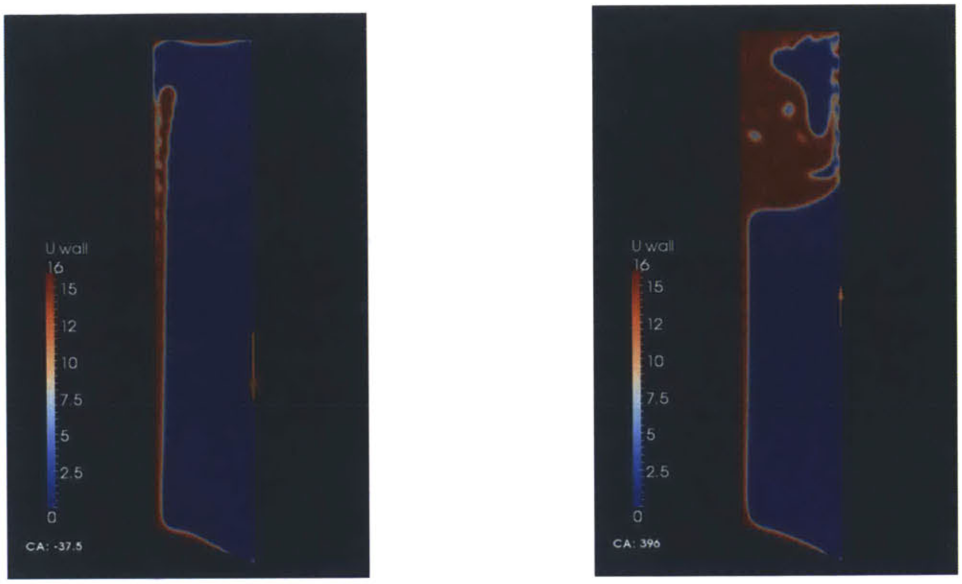

(a) Drop impact

(b) Vortex influence

is expected to be similar.

4.4 Conclusions for pressure effects

The conclusions for the pressure at the groove inlet are:

- hydrostatics are the main pressure effect at the groove inlet and do not vary between both cases due to vortices limiting the effective hydrostatic height
- other pressure effects due to changes in interface curvature or the impact of oil drops close to the groove inlet can be of same order of magnitude as the hydrostatic effect, but happen only for very short instants and do not matter much for oil transport into the groove
- after the oil is inside the groove flank, it is mainly driven by capillary action

4.5 Bridging

For analyzing bridging effects, it is useful to split the amount of oil inside the land into a base layer and an additional puddle (AP), which can move around, as shown

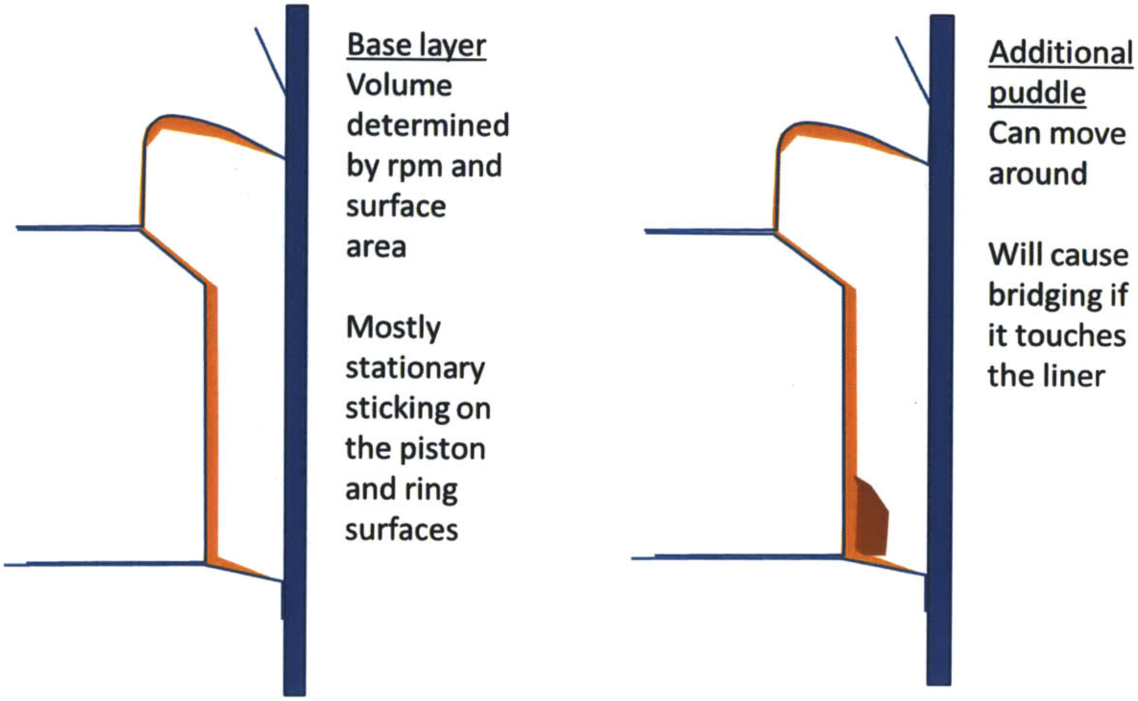

Figure 4-7: Base layer and additional puddle

in figure 4-7. The base layer height can be estimated using Tian's relationship [10]

$$h_{base} = \sqrt{\frac{S_p \nu_{oil}}{8V_{pmax}}} \tag{4.13}$$

and the area of the base layer is roughly

$$A_{base} = h_{base} \cdot H_{piston} \tag{4.14}$$

The remainder of oil area is the additional puddle, which can be assumed to be of triangular shape during movement, as previously simplified by Tian. Bridging happens if the additional puddle reaches the liner before TDC, after which the liner starts dragging air upwards and creates a high stagnation point at the second ring/liner corner which will prevent oil from touching the liner. The movement of the AP from the OCR towards the second ring can be divided into two parts: the drop movement on the piston towards the second ring and the spreading on the second ring flank, which are sketched in figure 4-8.

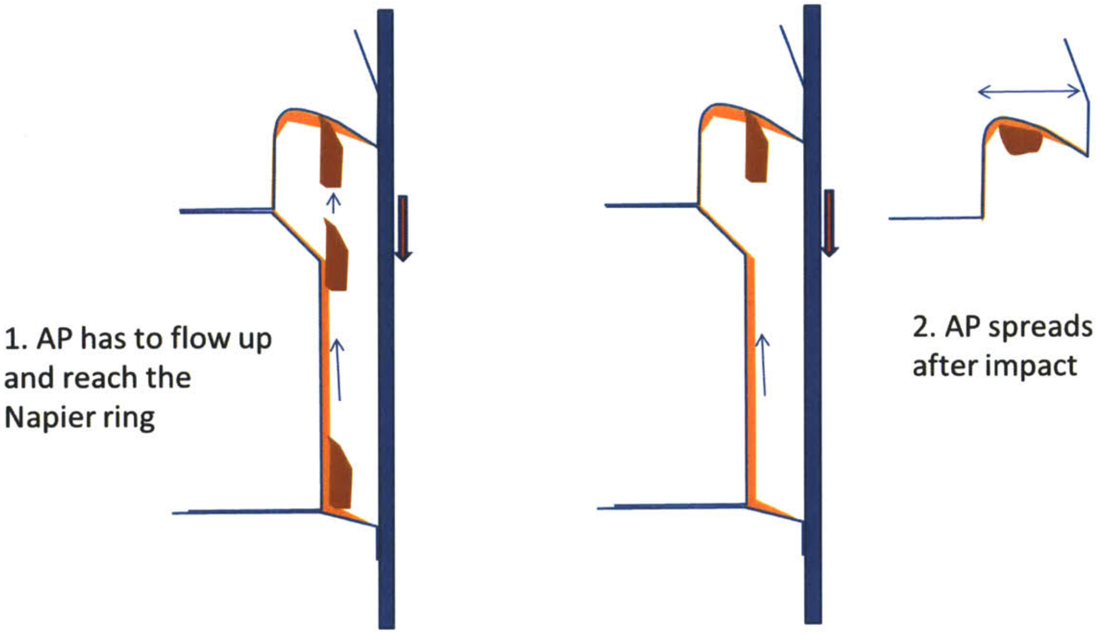

Figure 4-8: Bridging conditions

4.5.1 Oil drop flowing up the piston

Under the assumption of fully developed flow which is only driven by gravity, the Navier Stokes equation can be simplified to

$$\mu \frac{\partial^2 u_y}{\partial x^2} = -\rho g \tag{4.15}$$

with y being the coordinate parallel to the piston wall, which starts at the OCR, x the being normal component, which starts on the piston wall, and the boundary conditions

$$u|_{x=0} = 0, \ \frac{\partial u_y}{\partial x}|_{y=h_{AP}} = 0 \tag{4.16}$$

which yields a velocity of

$$u = \frac{\rho g}{\mu}\left(\frac{1}{2}x^2 + h \cdot x\right) \tag{4.17}$$

and an average velocity of

$$\bar{u} = \frac{1}{h}\int_0^{h_{AP}} u dx = \frac{\rho g h_{AP}^2}{3\mu} \tag{4.18}$$

The location on the piston can be simplified to $y(t) = \bar{U} \cdot t$ with a constant gravity which will flightly over-predict the result. This relationship is plotted against the simulated CFD results in figure 4-9, where the analytic solution is still lower than the simulation values. The results get closer as oil heights increase, which indicates a possible uncertainty in the estimation of base height. As oil heights increase, the base height remains unchanged for constant RPM and as $h_{AP}/hbase$ become larger, the influence of h_{base} decreases. Moreover there is also an influence from inertia since the Reynolds number

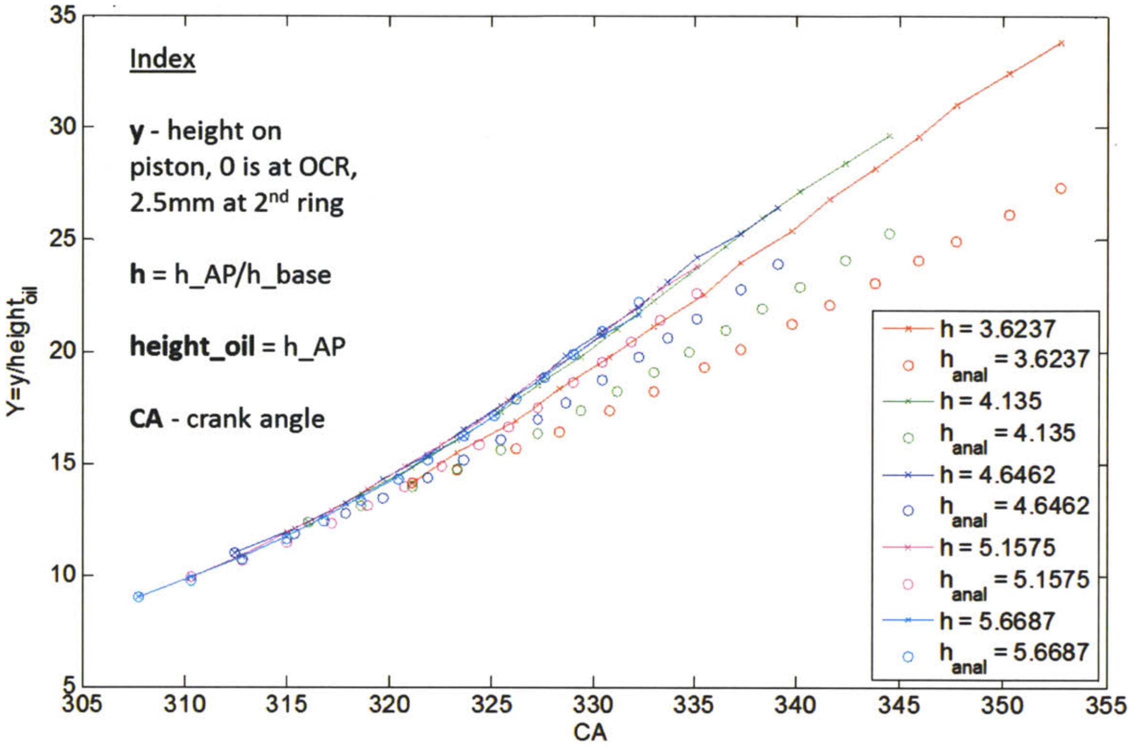

Figure 4-9: Oil drop positions on the piston

$$Re_L \left(\frac{H}{L}\right)^2 = \frac{u(h_{base} + h_{AP})^2}{\nu H_{piston}} \sim \frac{10^0 10^{-8}}{10^{-5} 10^{-3}} = 10^1 \tag{4.19}$$

indicates that the flow is not fully developed, which would prevent the possibility of deriving an analytical solution. Future work should attempt to include unsteady and inertia effects for a more exact description.

4.5.2 Spreading at the second ring

The duration of an impact is determined by the AP size and the impact velocity. A scaling analysis can show which effects are driving the spreading and how AP size and impact velocity can influence the effects. Using sketch 4-10 and the steady state momentum equation, the terms at spreading are

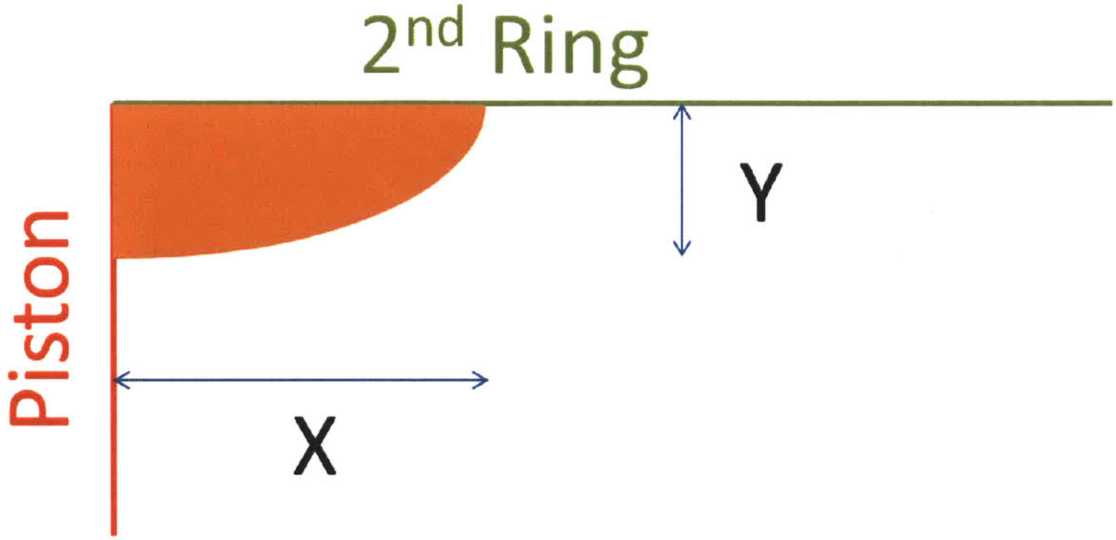

Figure 4-10: Spreading parameters

- inertia, which scales as $U\dfrac{U}{X}$
- viscous effects, which scale as $\nu\dfrac{U}{Y^2}$
- pressure effects due to interfacial tension, which scale as $\dfrac{\Delta p}{\rho X} = \dfrac{\frac{\sigma}{Y}}{\rho X}$

Unsteady effects are neglected because the impact duration is of much smaller magnitude as the cycle time. Based on the findings of section 4.5.1 the impact velocity can be of order 10^0 or 10^{-1} and the oil film thickness Y can be of order 10^{-5} or 10^{-4}. At impact, the length scales X and Y are of same order of magnitude. This leads to 4 possible impact scenarios:

- large AP with high impact velocity

- small AP with high impact velocity
- small AP with low impact velocity
- large AP with low impact velocity, which is not observed during any simulations because AP heights of the order 10^{-4} always result in impact velocities of the order 10^0

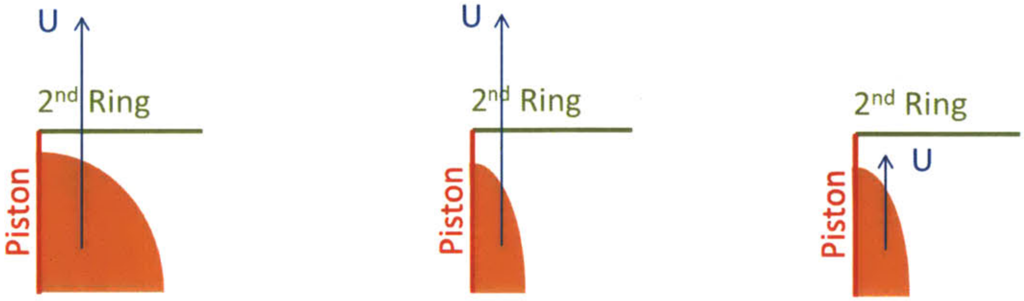

1. Large AP at high velocity hits the 2nd ring

2. Small AP at high velocity hits the 2nd ring

3. Small AP at low velocity hits the 2nd ring

Figure 4-11: Impact scenarios

The 3 different impact scenarios are sketched in figure 4-11 and further scaling for each case shows the dominant effects during impact:

1. High inertia large AP
    - Inertia $\sim 10^0 \frac{10^0}{10^{-4}} = 10^4$
    - Viscous effects $\sim 10^{-5} \frac{10^0}{(} 10^{-8} = 10^3$
    - Capillary effects $\sim \frac{10^{-2}}{10^3 10-410-4} = 10^3$
    - $\rightarrow Re = 10,\ Ca = 1,\ We = 10$
    - **Inertia driven spreading**
2. High inertia small AP
    - Inertia $\sim 10^0 \frac{10^0}{10^{-5}} = 10^5$

   - Viscous effects $\sim 10^{-5}\frac{10^{0}}{(}10^{-10} = 10^{5}$
   - Capillary effects $\sim \frac{10^{-2}}{10^{3}10-510-5} = 10^{5}$
   - $\rightarrow Re = 1,\ Ca = 1,\ We = 1$
   - **2 phase spreading**

3. Low inertia small AP
   - Inertia $\sim 10^{-1}\frac{10^{-1}}{10^{-5}} = 10^{3}$
   - Viscous effects $\sim 10^{-5}\frac{10^{-1}}{(}10^{-10} = 10^{4}$
   - Capillary effects $\sim \frac{10^{-2}}{10^{3}10-510-5} = 10^{5}$
   - $\rightarrow Re = 0.1,\ Ca = 0.1,\ We = 0.01$
   - **Crawling**

For inertia driven spreading, the incoming fast AP is not slowed down at all and quickly reaches the liner in under 10 crank angles after impact. In 2 phase spreading, the viscous forces and surface tension that is trying to minimize surface energy are able to reduce the velocity of the incoming fast AP by one order of magnitude and cause the spreading to enter the crawling scenario, for which the wetting of the surface will cause the interface to continue spreading at a velocity order of magnitude of $10^{-1}m/s$. Previous results for the spreading, for example shown by Leger et al [5], do not fit the simulation values that are gained in this study and further analytical work needs to be done in describing the spreading mechanism for a fully functional model. This is mainly complicated because of

- wetting at the corner, which dilutes the base height at the corner
- the continuity of the AP, which creates a continuous oil supply to the second ring even after impact
- the uncertainties as described in section 4.5.1

- the influence of all terms in the momentum equation which make simplifications and the derivation of an analytic expression difficult

4.5.3 Geometric variations

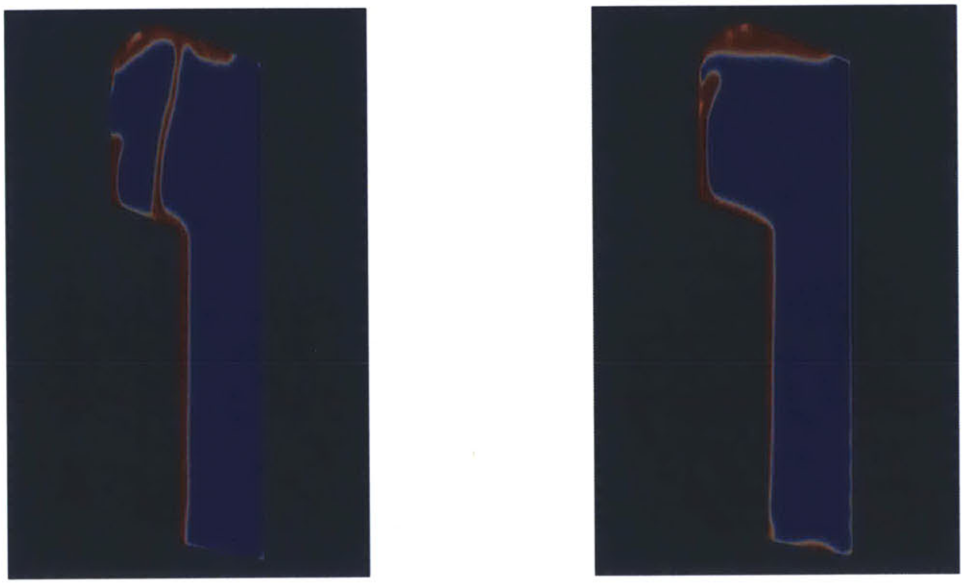

(a) Spreading into two directions

(b) Lake forming at the hooked ring

The previous analysis was based on a rectangular ring. Having negative angles α of the ring helps in preventing bridging due to gravitational effects. Similarly it makes bridging with positive angles easier, although the increase in travel distance due to the angle can negate the gravitational effect.

Having a hooked second ring and a chamfer significantly increases the amount of oil needed to bridge because oil can spread in both directions and thus reduces the effects oil amount that flows towards the liner as shown in figure 4-12a and the hook creates a lake that will store oil as gravity and surface tension try to keep a flat shape of the surface of the lake, as shown on figure 4-12b. The resulting bridging map in figure 4-12 shows the influence of angle variation and design change. For the hooked ring with chamfer setup, almost double the amount of oil is needed to bridge.

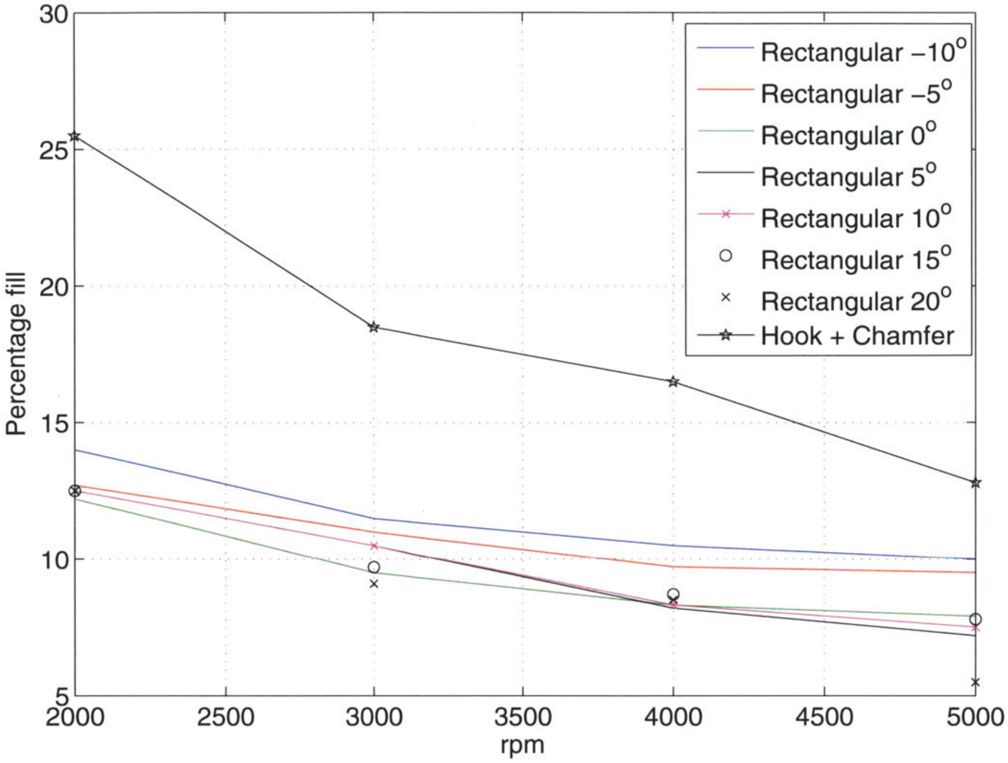

Figure 4-12: Bridging map

4.5.4 Bridging height

Under the assumption that bridged oil sticks to the liner and gets dragged down with liner velocity as shown in figure 4-13, the bridging height can be calculated by integrating the piston velocity from the crank angle at which bridging happens to TDC

$$\begin{aligned} h_{bridged} &= \int_{CA_{bridge}}^{CA_{TDC}} u_{liner} dCA \\ &= r\left(\cos\left(CA_{bridge}\right) - \cos\left(CA_{TDC}\right)\right) \\ &+ \sqrt{l^2 - r^2 \sin^2\left(CA_{bridge}\right)} - \sqrt{l^2 - r^2 \sin^2\left(CA_{TDC}\right)} \end{aligned} \tag{4.20}$$

which has less than 1% difference from the simulation value. Thus it is the time between TDC and bridging instant that determines the bridging height.

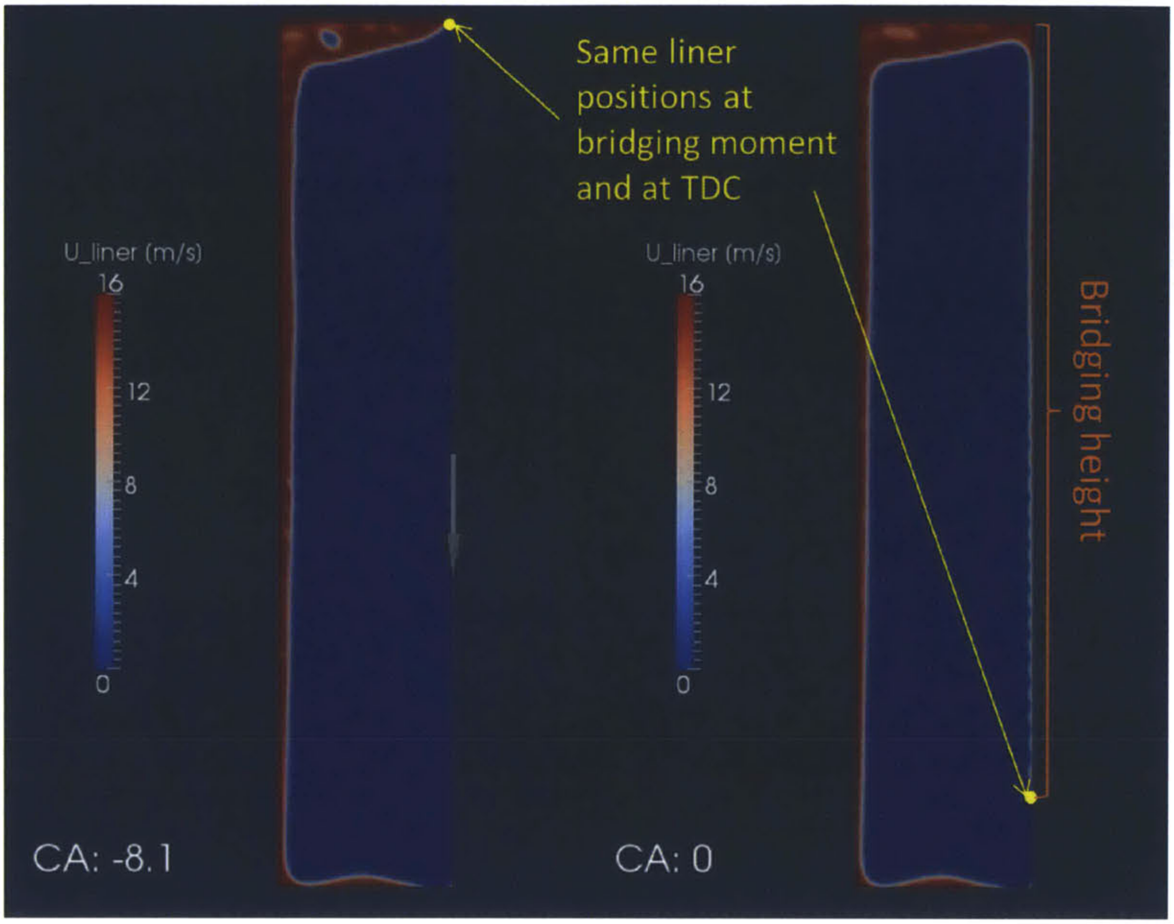

Figure 4-13: Bridging height

4.6 Conclusions for bridging

The analysis of bridging in this work can finally be summed up with

- the crank angle, at which an additional puddle reaches the second ring depends on rpm and the puddle size
- the condition at which the AP arrives at the second ring leads to 3 impact scenarios
  - high inertia large AP impact scenarios do not allow viscous action or surface effects to slow down the spreading, thus the AP will almost immediately hit the liner after impact on the second ring
  - small APs at large rpm are slowed down after impact due to viscous stresses

  and surface tension trying to minimize surface energy. After velocity is slowed down by one order of magnitude, the spreading will go into the crawling scenario

  - small APs at low rpm are crawling at the very beginning of impact and approach the liner with a velocity in the order of $10^{-1} m/s$

- the height of bridged oil depends on how much time is left before TDC at bridging

- positive ring angles favor bridging while negative angles prevent oil from touching the liner

- the best prevention of bridging is by using a hooked design with chamfer which will almost double the amount needed to bridge

Chapter 5

Summary

In the 3 different blowby flow regimes, the main influence of air on oil transport are close to gaps and directly below the ring-liner contacts. At the gaps,

- only oil, that is within 1 to 2 gaps widths distance from the gap, is sucked downstream
- blowby can be controlled by geometry design, which has a direct proportional influence on oil drain inside the OCR groove
- vortices, whose strengths and sizes can be controlled by Mach-number and choking conditions, cause oil accumulation
- oil is pumped directly into the groove due to high pressure at the stagnation points on the downstream rings

Far away from the gaps

- most of blowby is passing through the groove due to lower shear inside the grooves
- air mass flow rate is determined by the pressure gradient in either circumferential direction
- air has almost no effect on oil, except in the prevention of bridging after TDC

- oil is mainly transported in axial direction through the grooves and ring-liner interfaces, whereas circumferential transport in the second land can be almost neglected due to very low flow velocities

Bibliography

[1] E. M. Greitzer, C. S. Tan, and M. B. Graf. *Internal Flow: Concepts and Applications (Cambridge Engine Technology Series).* Cambridge University Press, 2007. 21, 28, 58

[2] John Heywood. *Internal Combustion Engine Fundamentals.* McGraw-Hill Science/Engineering/Math, 1988. 61

[3] H. Jasak. *Error analysis and estimation for the Finite Volume method with applications to fluid flows.* PhD thesis, Imperial College, University of London, 1996. 31

[4] Pijush K. Kundu, Ira M. Cohen, and David R Dowling. *Fluid Mechanics.* Academic Press, 2011. 54

[5] L Leger and J F Joanny. Liquid spreading. *Reports on Progress in Physics*, 55(4):431, 1992. 77

[6] T. J. Poinsot and S. K. Lele. Boundary conditions for direct simulations of compressible viscous flows. *Journal of Computational Physics*, 101:104–129, July 1992. 46

[7] Lord Rayleigh. On the dynamics of revolving fluids. *Proceedings of the Royal Society of London. Series A*, 93(648):148–154, 1917. 50

[8] E. B. Senzer. *Oil Transport Inside the Oil Control Ring Groove and Its Interaction with Surrounding Areas.* PhD thesis, Massachusetts Institute of Technology, 2012. 19, 43

[9] Ascher H. Shapiro. *The Dynamics and Thermodynamics of Compressible Fluid Flow, Vol. 1.* Wiley, 1953. 19

[10] T. Tian. Oil consumption and oil transport. Presented at the MIT Sloan Automotive Laboratory Consortium for Lubrication in July 2011, 2011. 72

[11] T. Tian, L. B. Noordzij, V. W. Wong, and J. B. Heywood. Modeling piston-ring dynamics, blowby, and ring-twist effects. *Journal of Engineering for Gas Turbines and Power*, 120:843–854, October 1998. 19, 42

[12] A. J. Ward-Smith. *Internal Fluid Flow: The Fluid Dynamics of Flow in Pipes and Ducts.* Oxford: Clarendon Press, 1980. 23